Nanophotonic Visible Light Phased Arrays

by

Manan Raval

B.S. Electrical Engineering
University of Illinois at Urbana-Champaign (2014)

Submitted to the
Department of Electrical Engineering and Computer Science
in Partial Fulfillment of the Requirements for the Degree of

Master of Science in Electrical Engineering and Computer Science
at the
Massachusetts Institute of Technology

September 2016

Signature redacted

Signature of Author .....
Department of Electrical Engineering and Computer Science
August 31, 2016

Signature redacted

Certified by.....
Michael R. Watts
Associate Professor
Thesis Supervisor

Signature redacted

Accepted by .....
Leslie Kolodziejski
Chair, Department Committee on Graduate Students

Nanophotonic Visible Light Phased Arrays

by

Manan Raval

Submitted to the Department of Electrical Engineering and Computer Science
On August 31, 2016 in Partial Fulfillment of the
Requirements for the Degree of Master of Science in
Electrical Engineering and Computer Science

Abstract

Previously demonstrated integrated optical phased arrays have primarily been implemented in silicon-based platforms and have therefore been limited to operation at infrared wavelengths, where silicon provides low-loss transmission. Developing integrated optical phased arrays for visible wavelengths would enable the exploration of new applications for this technology, such as autostereoscopic displays and neuronal targeting for optogenetics. The work presented in this thesis involves the development of visible light integrated optical phased array components and systems with a focus on autostereoscopic image projection applications.

Practical 3D microdisplay applications will require (1) large-aperture phased array systems for diffraction minimization, (2) integrated phase modulation for implementing dynamically reconfigurable phased array antenna elements, and (3) a phased array system architecture for accurately encoding the light field of virtual objects. Integrated photonic architectures for all three aforementioned goals are investigated in this thesis. With respect to the first goal, a 1×1 mm^2 aperture visible light phased array with a near diffraction limited far-field spot size is demonstrated. With respect to the second goal, the design of an integrated phase modulator based on the electro-optic tuning of a nematic liquid crystal waveguide cladding layer is developed and a near-π phase shift is demonstrated in a fabricated device. Finally, an autostereoscopic image projection system comprised of multiple tiled phased arrays configured to project a virtual image with parallax in one dimension within an 8.58° field of view is demonstrated.

Thesis Supervisor: Michael R. Watts
Title: Associate Professor

Acknowledgements

I would first like to thank my advisor, Professor Michael Watts, who provided me with the opportunity and the resources to carry out the work presented in this thesis. His guidance and insights consistently aided in determining the direction of my research. Facilitated by Prof. Watts, my project has led me through a diverse set of research experiences which have been instrumental in my development as both an independent and collaborative researcher.

Working with the members of the Photonic Microsystems Group has been a delight and an honor. My work began as a continuation of Ami Yaacobi's PhD research. The work presented in this thesis would not have been possible without his mentorship when I joined the group and his encouragements at times when I felt my work was at a standstill.

A vast amount of technical knowledge passed down to me by Erman Timurdogan and Zhan Su has enabled many of the research ideas I explored over the past two years. I am constantly in awe of the persistence they show in their research and I sincerely thank them for the invaluable influence they've had on my work and my growth as a researcher.

Christopher Poulton, who joined the lab when I did, has been a great friend and labmate. Frequent discussions about research ideas as well as his insights into photonic device design were extremely helpful throughout the past two years.

An appreciable portion of this past year was spent writing a fairly ambition grant proposal. I'd like to thank Diedrik Vermeulen for guiding the proposal writing effort and helping to refine the ideas presented therein. His knowledge and intuition of integrated photonics as well as his dedication to his work are indispensable for the lab as a whole and were crucial throughout the writing process.

Outside the lab, my friends were the first line of defense against the looming stresses of graduate school. To Sam Beller, Clark Wood, Juliana Nazare, Coleman

Mahler, Jacob Guggenheim, Ashvin Bashyam, and many others, thank you for keeping me grounded and putting up with my bad jokes for over two years now.

Finally, I'd like to thank my parents. I would not have made it this far were it not for their sacrifices and their unconditional love and support. I love you both very much. This thesis is dedicated to you.

Contents

List of Figures

1 Introduction

The phased array, the invention of which is attributed to Nobel laureate Karl Ferdinand Braun, is an apparatus comprised of an array of antennas, the amplitudes and phases of which are controlled to shape the emitted radiation [1]. Phased arrays are capable of emitting highly directional radiation that may be steered by appropriately tuning the relative phases of its antenna elements. For several decades, radio frequency phased arrays have seen widespread use for radio detection and ranging (RADAR) and broadcasting applications [2]. While RF phased array technology has achieved relative maturity, high system complexity and manufacturing costs arising from the need for discrete mechanical components have rendered the development and deployment of large-scale systems generally impractical. Compact non-mechanical low-cost phased array systems are therefore highly desirable. The advent of highly accurate silicon photonics fabrication technology in recent years has provided a platform in which arrays of compact antennas operating at optical wavelengths may be implemented on a single chip in a high volume manufacturing process, thereby satisfying the aforementioned requirements of the ideal phased array system. Operating in the optical domain also affords higher resolution for imaging and ranging applications as compared to the RF domain given the significantly shorter emission wavelength. Optical phased arrays have therefore been widely investigated for light detection and ranging (LIDAR) applications [3-6].

The majority of integrated optical phased arrays demonstrated to date have been implemented in silicon-based platforms and have largely been limited to operating in the C- (1530-1565 nm) and L-bands (1565-1625 nm), where silicon provides low loss transmission [5-8]. Expansion into the visible spectrum would enable integrated optical phased array technology to address previously unexplored application spaces

requiring visible wavelengths such as chip-scale autostereoscopic 3D displays [9-10] and neuronal targeting for optogenetics [11]. In view of this motivation, the work presented in this thesis was carried out with two primary goals. The first was to develop an infrastructure of photonic components in a silicon nitride platform for the realization of large-scale visible light phased arrays. The second was to investigate the use of integrated phased array systems for autostereoscopic 3D microdisplay applications. The remainder of the introduction will be devoted to providing an overview of phased array theory and architecture as well as a brief analysis of current autostereoscopic display methods. Following this, the second chapter will detail the design and demonstration of autostereoscopic image projection using a system of integrated optical phased arrays for generating a virtual image with parallax in one dimension. The third chapter details the design and characterization of large-aperture phased arrays. Finally, the fourth chapter discusses the use of nematic liquid crystals for phase modulation and the development of an integrated visible light phase modulator using a liquid crystal waveguide cladding layer.

1.1 Optical Phased Array Theory

The intensity distribution of the emitted wave in the far-field of a phased array results from the mechanism of wave interference, governed by the superposition principle. Fig. 1.1(a) illustrates the operational concept of a phased array, in which the complex emission w of each antenna may be expressed as

$$w_i = A_i e^{j\varphi_i} \tag{1.1}$$

where A_i and φ_i are amplitude and phase of the i^{th} antenna, respectively. In its simplest form, a phased array is configured such that each of the equally spaced antennas emits with the same phase and amplitude. In this case, the superposition of the emitted electromagnetic waves results in a pronounced intensity maximum in the far field, which may be treated as a directional beam, as shown in Fig. 1.1(c). As

shown in Fig. 1.1(b), an angled phase front is produced if a uniform relative phase shift $\Delta\phi$ is added between each antenna, resulting in steering of the beam by angle θ. This is represented in the far-field radiation pattern as well, as shown in Fig. 1.1(d).

The far field of a one-dimensional phased array can be generally expressed as

$$E(\theta) = \sum_{n=1}^{N} \omega_n e^{-j\mathbf{k_n}\cdot\mathbf{r_n}} = \sum_{n=1}^{N} \omega_n e^{-j\mathbf{k}\cdot\mathbf{r_n}} = \sum_{n=1}^{N} \omega_n e^{j(\frac{2\pi}{\lambda})x_n \sin\theta} \tag{1.2}$$

where $\mathbf{k_n}$ is the wavevector originating from the n^{th} antenna, $\mathbf{r_n}$ is the spatial vector representing the path from the n^{th} antenna to a point in the far field, $\mathbf{k}$ is the wavevector originating from the center of the phased array, ω_n is the complex amplitude of emission of the n^{th} antenna, x_n is the spatial location of the n^{th} antenna, and λ is the wavelength of the emitted electromagnetic radiation. The first of the above equalities, which establishes the assumption that $\mathbf{k} \approx \mathbf{k_1} \approx \mathbf{k_2} \approx \mathbf{k_n}$, holds true in the far field, where $D << L$, where D is the total dimension or aperture of the phased array and L is the distance away from the phased array. The approximate distance L_f at which the far field is formed is known as the Fraunhofer distance and can be expressed as

$$L_f = \frac{2D^2}{\lambda} \tag{1.3}$$

It should be noted that a phased array will only emit a single beam or specific far-field radiation pattern if the antenna pitch d is less than $\lambda/2$. Higher orders of emission are seen when the pitch exceeds this value, as shown in Fig. 1.1(e-f). Higher orders are generally undesirable since they carry redundant information and limit the k-vector domain of the fundamental order. For instance, for an application requiring beam steering, this directly translates to a decrease in the maximum steering range of the phased array.

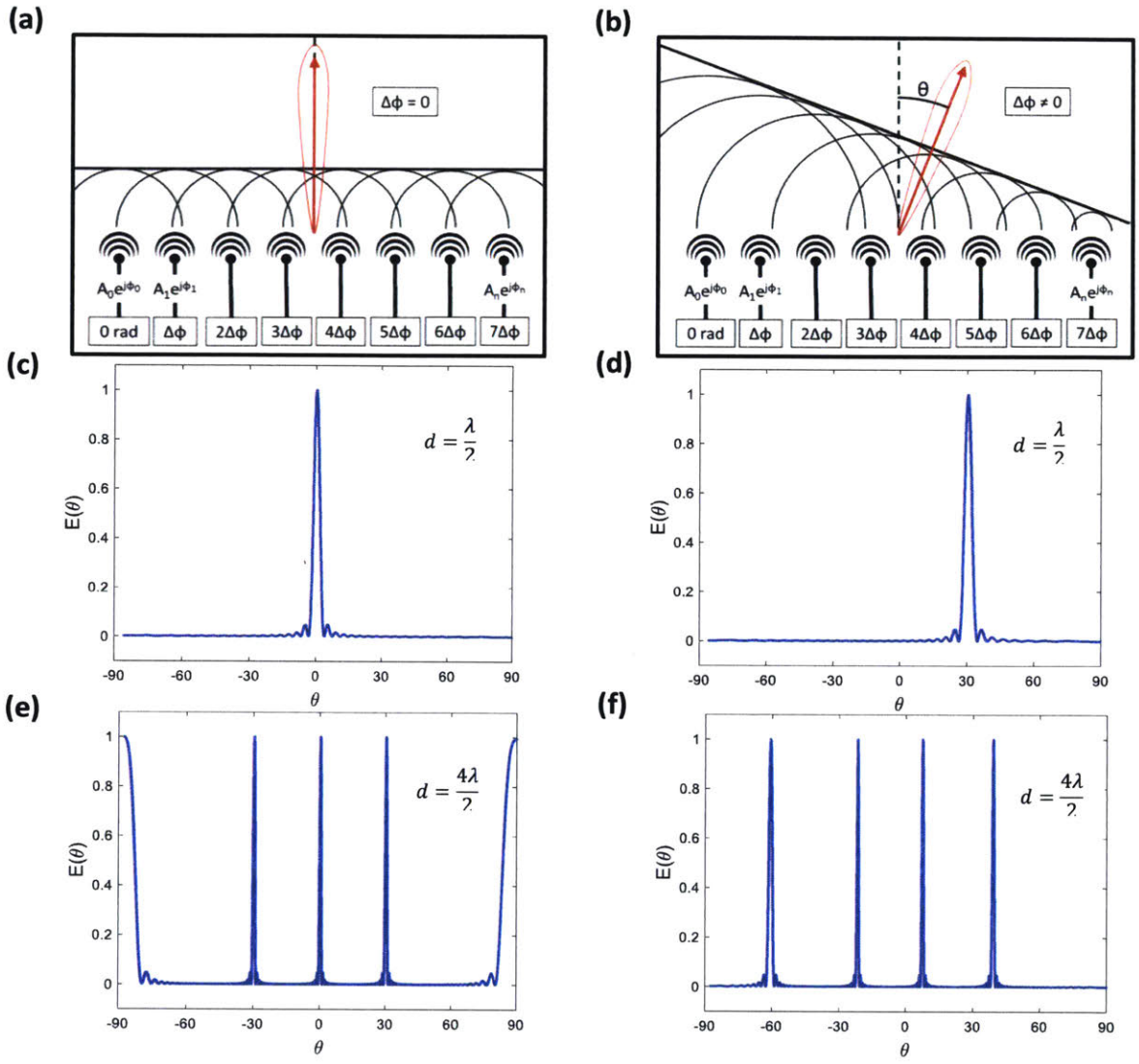

Figure 1.1 (a) Phased array concept with uniform phase and amplitude distribution. (b) Phased array with relative phase shift between antennas resulting in a steered phase front. (c-d) Initial and steered far fields with antenna spacing d = λ/2. (e-f) Initial and steered far fields with antenna spacing d = 4λ/2.

The far-field of a phased array expressed in Equation 1.2 is also referred to as the Array Factor if each antenna is treated as an ideal point source [12-13]. The array factor $AF(\theta,\phi)$ in two dimensions is written as

$$AF(\theta,\phi) = E(\theta,\phi) = \sum_{m=1}^{M}\sum_{n=1}^{N} \omega_{mn} e^{j\left(\frac{2\pi}{\lambda}\right)(x_m \cdot \sin\theta\cos\phi + y_m \cdot \sin\theta\sin\phi)} \tag{1.4}$$

As seen in Equation 1.4, the amplitude and phase of each antenna in the phased array is a degree of freedom that may be arbitrarily controlled to generate more complex far-field radiation patterns. For instance, a 64×64 unit cell integrated optical phased array was demonstrated with a very specific phase configuration passively encoded into the antennas such that the MIT logo would be formed in the far field [5]. This phased array, which was implemented in a silicon-on-insulator (SOI) platform and had uniform distribution of 1550 nm optical power to each antenna, was also the largest optical phased array demonstrated to date. Another integrated optical phased array architecture in which the antenna phases were configured for optical orbital angular momentum generation has also been demonstrated [14-15].

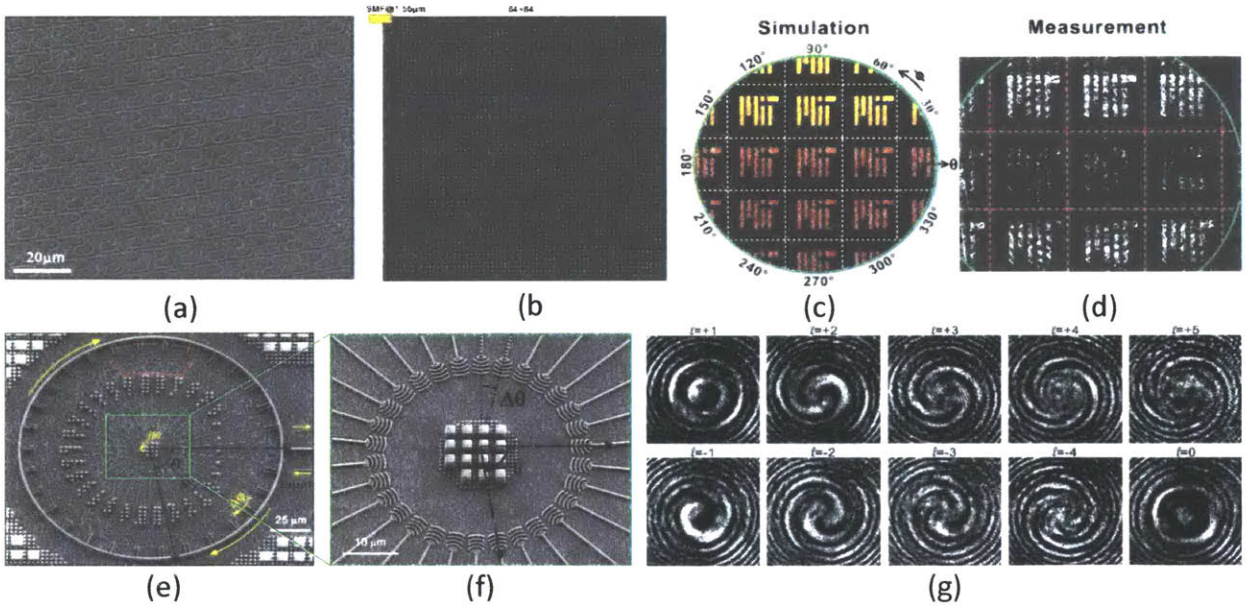

Figure 1.2. 4,096 unit-cell passive phased array: (a) SEM image. (b) Near-field emission. (c) Simulated and (d) measured far-field radiation patterns. Reconfigurable Orbital Angular Momentum (OAM) generator: (e-f) SEM image of emitter configuration. (g) Emitted beams with varying vortex charge.

Fraunhofer diffraction theory shows that the far-field of a linear time-invariant optical system is the Fourier transform of the near field multiplied by a curved phase front [13]. According to the paraxial approximation, this phase front has a parabolic curvature for small angles. A Fourier analysis of the phased array system described by Equation 1.4 is extremely useful for the design of large scale phased arrays for arbitrary far-field pattern generation. The array factor may be represented as a discrete Fourier transform upon carrying out a coordinate transformation in Equation 1.4 as follows

$$u = \frac{\sin\theta\cos\phi}{\lambda}, \qquad v = \frac{\sin\theta\sin\phi}{\lambda} \tag{1.5}$$

$$AF(u,v) = F(\omega_{mn}) = \sum_{m=1}^{M}\sum_{n=1}^{N} \omega_{mn} e^{j2\pi(x_m \cdot u + y_m \cdot v)} \tag{1.6}$$

If each antenna in the phased array is assumed to be an ideal point source, the near field may be mathematically expressed as a 2D Dirac comb multiplied by a continuous complex amplitude function *g(x,y)* representing the phase and amplitude encoding of the antennas as follows

$$e(x,y) = g(x,y) \times \sum_{m=-\infty}^{\infty}\sum_{n=-\infty}^{\infty} \delta(x - x_m, y - y_n) \tag{1.7}$$

The expression for the far-field obtained upon carrying out a Fourier transform is

$$\begin{aligned} AF(u,v) &= F[e(x,y)] = F[g(x,y)] \otimes F\left[\sum_{m=-\infty}^{\infty}\sum_{n=-\infty}^{\infty} \delta(x - x_m, y - y_n)\right] \\ &= G(u,v) \otimes \sum_{m=-\infty}^{\infty}\sum_{n=-\infty}^{\infty} \delta\left(u - m\frac{2\pi}{d_x}, v - n\frac{2\pi}{d_y}\right) \end{aligned} \tag{1.8}$$

The above expression reiterates that the far-field pattern will include higher orders if $d_{x,y} > \lambda/2$. Furthermore, since both u and v are bounded by $[-1/\lambda, 1/\lambda]$, the number of far-field periods in a given dimension will be

$$N_{u,v} = \frac{2d_{x,y}}{\lambda} \tag{1.9}$$

Given full control of both the amplitude and phase of each antenna in a phased array, determining the necessary near field for a given desired array factor is simply a matter of encoding the phased array with its inverse Fourier transform. Unfortunately, it remains a challenge to implement integrated optical phased arrays with full amplitude and phase control. Typically, the amplitude $|w_{mn}|$ is kept uniform over the entire array while the phase of each antenna is adjusted. The loss of this degree of freedom may be compensated by the fact that the phase distribution of the array factor is of no importance and may be set to any value since only the amplitude distribution of the array factor is relevant. The near-field phase distribution may then be found using an iterative algorithm which allows complete freedom in the far-field phase distribution while limiting the near-field and far-field amplitude distributions. A modified version of the Gerchberg-Saxton (GS) algorithm, often used in holography, has been demonstrated for this purpose [16]. A diagram of the modified GS algorithm is shown in Fig. 1.3.

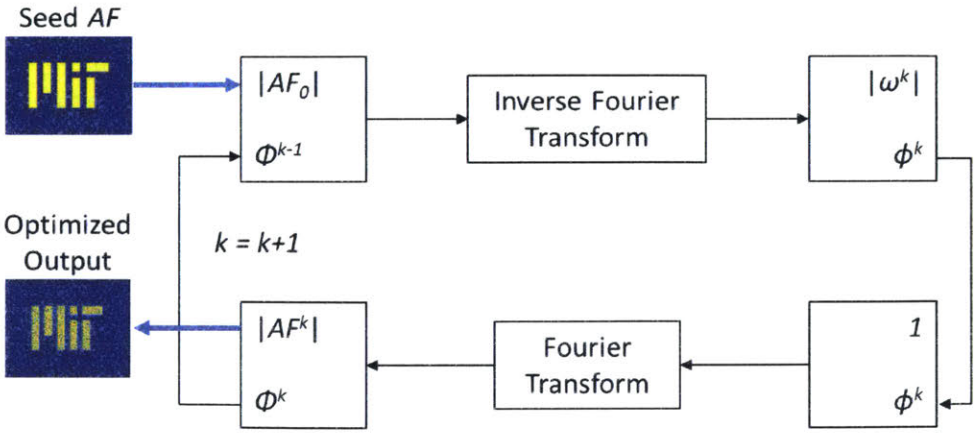

Figure 1.3. Gerchberg-Saxton Algorithm flowchart.

The GS algorithm begins with taking the inverse Fourier transform of an initial seed array factor consisting of the desired amplitude distribution and a random phase distribution. The resulting near-field amplitude distribution is discarded and the amplitudes of all antennas are set to unity while the near-field phase distribution is retained. The Fourier transform of this near field is taken to yield the array factor AF^k of the current iteration. The seed array factor AF^{k+1} for the subsequent iteration is formed by combining the phase distribution from the previous iteration and the target amplitude distribution. The algorithm iterates until the amplitude of the output array factor $|AF^k|$ converges to the target amplitude distribution. The antenna phase distribution of the previously mentioned phased array configured to project the MIT logo was determined using the GS algorithm. This algorithm will also be used for determining the necessary phase distribution of the visible light integrated optical phased arrays that will be discussed in Section 2.2 of this thesis.

1.2 Optical Phased Array Architecture

An optical phased array is comprised of three primary components: (1) an optical distribution system for directing appropriate fractions of the optical power from a common coherent source to each antenna, (2) a phase modulation mechanism in each antenna unit cell for controlling its relative phase, and (3) optical antennas for coupling to free space. This section provides a brief high-level overview of possible designs for these components while the devices discussed in the following chapters use specific implementations of these components for different phased array architectures.

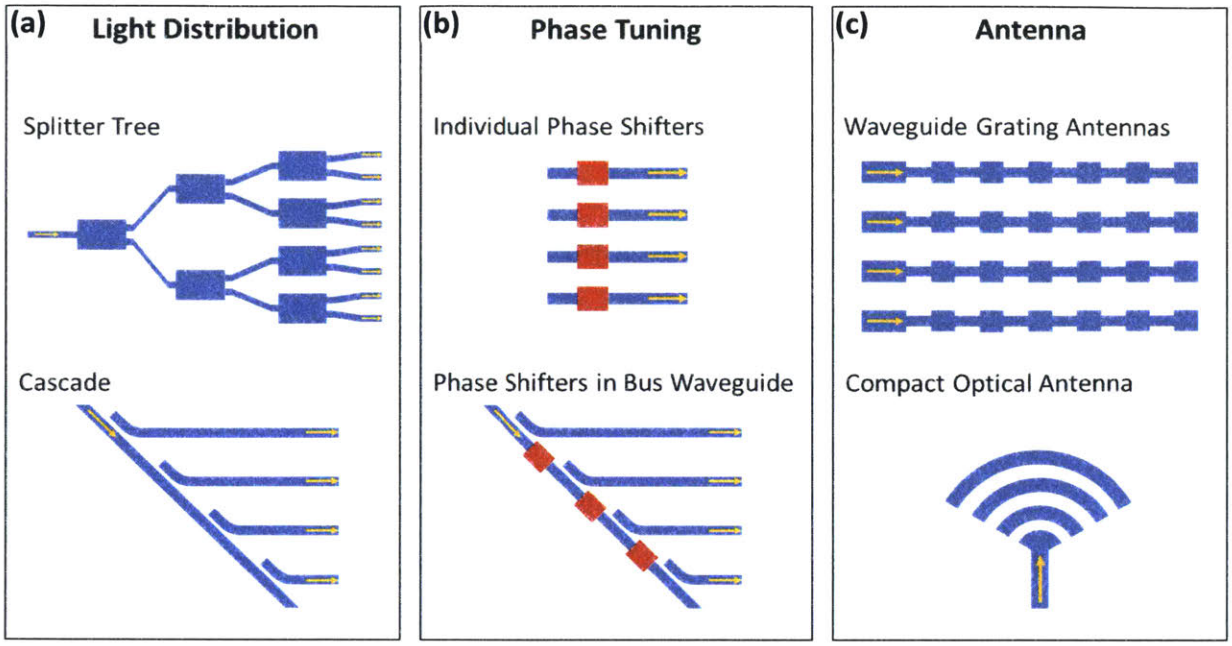

Figure 1.4. Overview of potential implementations of the three primary components of an integrated optical phased array.

Distribution of light is generally carried out using either a tree of 1×2 splitters, such as MMI couplers or Y-splitters, or in a cascaded manner with a series of directional couplers for tapping the appropriate amount of light from a bus waveguide [3,6,7]. A schematic of these two splitting methods is shown in Fig. 1.4(a). A 1×N star coupler may also be used, but this design often results in phase non-uniformity at the output and is difficult to scale up since fabrication errors become more pronounced when N is large [17]. Either architecture may be used for 1D phased arrays, but 2D phased arrays generally require cascaded light distribution in at least one dimension.

The phase modulation mechanism may be placed within the unit cell or, in the case of a cascaded distribution system, within the bus waveguide between the directional couplers for adjacent unit cells. These two phase modulation schemes are illustrated in Fig. 1.4(b). For arbitrary far-field pattern generation, it is necessary to have independent control of the phase modulator associated with each antenna, but simpler phase modulator addressing schemes may be implemented for tasks such as

beam-steering. For instance, a cascaded distribution system would allow every modulator to be controlled using a single signal for beam-steering since this task requires a constant relative phase shift between adjacent antennas. This is not possible for a phased array using a tree structure because the correct absolute phase must be individually encoded into each antenna.

Optical antennas are generally grating based antennas, but 1D and 2D phased arrays require different designs. For generating a small spot using a 1D phased array, the aperture must be large in both dimensions. A long waveguide grating antenna, as shown in Fig. 1.4(c), is used to implement a large-aperture phased array with 1D light distribution and phase modulation. A 2D phased array with small pitch requires a compact emitter, as illustrated in Fig. 1.4(c), with a strong perturbation strength to couple as much light as possible to free space. As an example, the 64×64 unit cell passive phased array mentioned earlier for arbitrary far-field generation utilized a compact optical antenna for 1550 nm emission designed to occupy a 9 μm × 9 μm unit cell as seen in Fig. 1.2(a) [5].

1.3 Autostereoscopic Image Projection Methods

Autostereoscopic glass-free 3D displays are considered the ultimate goal of visualization technology. A true or perfect 3D display presents a scene with no distortions as compared to the desired physical objects being projected. In other words, a real-world scene duplicated by a perfect 3D display would exhibit no differences or deviations with respect to the original scene. More specifically, a scene projected by a perfect 3D display would provide all depth cues to the viewer. There are four physiological depth cues in the human visual system: accommodation, convergence, binocular disparity, and motion parallax [18]. Accommodation refers to the active deformation of the lens in the eye to focus to the plane of the object being viewed. Convergence is the action of the eyes pointing inward such that the line of

sight of the two eyes converge at the location of the object being viewed so as to triangulate its location. Convergence is necessary for objects close to the viewer (less than 10 meters away) but becomes less useful for faraway objects [19]. Binocular disparity, or stereopsis, refers to the two eyes perceiving two slightly different images due to their spatial separation. These two slightly different angular views further aid in the triangulation process involved in generating a final image by the human visual system. Motion parallax refers to the relative perceived movement of objects depending on their distance from the viewer. For instance, objects closer to the viewer will appear to move faster than those far away. Accommodation and motion parallax are monocular depth cues while convergence and binocular disparity are binocular depth cues. These four depth cues are illustrated in Fig. 1.5.

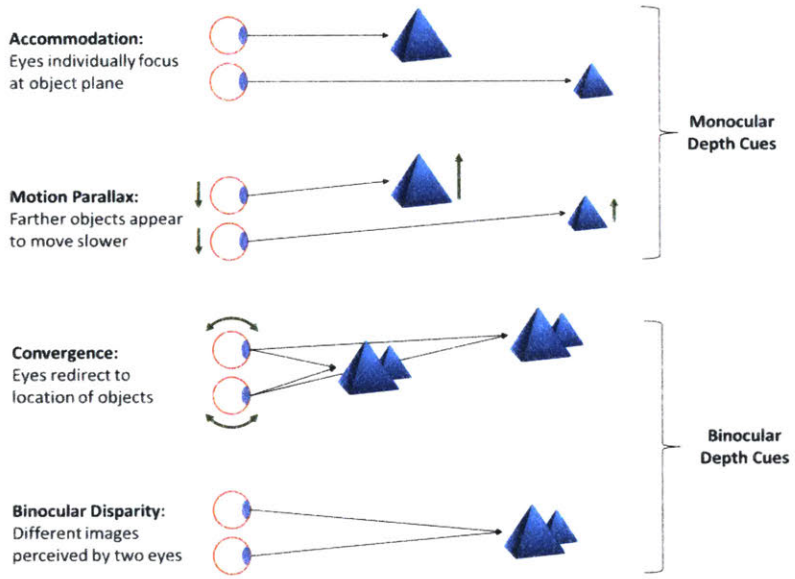

Figure 1.5. Physiological depth cues in the human visual system.

Holography is a method in which the exact wave front of a virtual 3D scene is recreated, but there are several challenges that holographic video must overcome for it to serve as a practical perfect 3D display solution [9,10]. One of the primary challenges facing dynamic digital holography is the limits on the spacing of controllable optical elements in electro-optic devices used for this application such as

a spatial light modulator (SLM). In SLM devices for phase and amplitude modulation based on liquid crystals and microelectromechanical systems (MEMS), pixel pitch lower than 2 μm has not yet been shown [20]. While this pitch is relatively low, it is significantly higher than the magnitude of visible wavelengths, thereby yielding higher order images and limiting the FOV in holographic systems [10]. Although lower pixel pitch technologies may be realized in the future, reasonably sized holographic displays with sub-micron pixel pitch may be comprised of multiple trillions of pixels and will require an amount of data and computation per frame that is unprecedented when compared to today's display technologies. Another issue facing holographic systems is that of speckle, which presents itself as a high contrast granular pattern in the image and arises due to random constructive and destructive interference of coherent light reflected from a rough surface [21-23].

While a digital holography system with the above issues resolved would provide ideal 3D displays, significant progress has been made in the development of incoherent methods for autostereoscopic 3D video. To provide an overview of incoherent autostereoscopic 3D displays, a selection of methods which have been widely researched in the last several years, including parallax barriers, lenticular sheets, integral imaging, and projection-based multi-view displays [9,10], will be discussed in the following material.

To understand the above methods, which are largely geometric optical methods, it is necessary to first understand the plenoptic function and representations of light fields. The plenoptic function, developed by Adelson and Bergen [24], is an observer-based characterization of the radiance along all light rays passing through a 3D space. A general form of the plenoptic function may be written as $P(x,y,z,\theta,\phi)$, which specifies a coordinate (x,y,z) at which incoming light is being received and a set of angles (θ,ϕ) representing the direction from which the incoming light is incident. The plenoptic function specifically demonstrates the necessity for directionally varying emitters for the accurate reconstruction of virtual 3D scenes using 2D display geometries. The plenoptic function may be reduced to a 4D light field representation

if there are no occluding objects present in the 3D space of concern [25]. The 4D light field may geometrically be represented as $L(s,t,u,v)$. The coordinates (s,t) and (u,v) represent points on two Cartesian planes. As shown in Fig. 1.6, these four parameters fully characterize the directionality of a ray passing through these planes [25]. In the limit that the z location of (u,v) approaches infinity, this coordinate subset may be replaced with spherical coordinates (θ,ϕ) to define the angular direction of the ray passing through point (s,t), leading to a reformulation of the 4D light field as $L(x,y,\theta,\phi)$. The goal of an autostereoscopic 3D display is to replicate the 4D light field of a 3D scene with the highest possible fidelity.

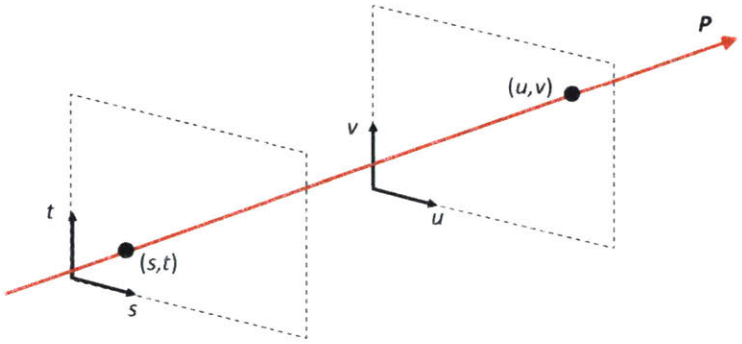

Figure 1.6. Two-plane representation of a 4D light field.

1.3.1 Parallax Barrier

A parallax barrier involves spatially blocking certain pixels or sections in a screen such that they are visible only from certain angles [26-27]. This may be done by placing an appropriately patterned occlusion mask a certain distance away from the display. An illustration of the action of a parallax barrier in one dimension is shown in Fig. 1.7 [10]. The encoding of directionality onto pixels is based on the fact that certain pixels are visible only from certain angles depending on the location of gaps in the overlying occlusion mask. Also, the extent of the overlap between view zones determined by the geometry of the parallax barrier must be properly engineered to provide continuous viewing across the entire field of view without introducing any

significant image blurring, which results from too much overlap between adjacent view zones [10]. Parallax barriers have several drawbacks. The first is that the number of apertures in the barrier layer determines the resolution for a given view. Therefore, for an N-view parallax barrier, the image resolution decreases by $1/N$. The capacity to generate a very limited number of views does not allow a continuous reproduction of the desired light field and may result in skewing of the projected depth cues. These inaccuracies are especially pronounced when transitioning between view zones, where the images intended for the left and right eye may be directed to the opposite eye, resulting in erroneous depth cues presented to the viewer. Since a mask must be placed directly above the display, a significant portion of the light emitted by the display is blocked, thereby reducing brightness. Also, an increase in resolution would inherently require a decrease in the size of apertures in the mask, which would increase the amount of diffraction and result in image blurring.

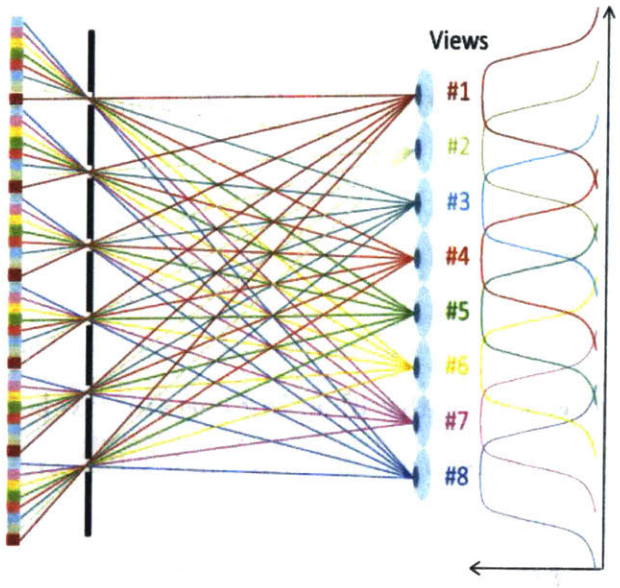

Figure 1.7. Schematic of a horizontal parallax only multi-view parallax barrier [10].

1.3.2 Lenticular Sheet

A lenticular sheet is comprised of a one dimensional array of plano-convex cylindrical lenses. When placed above a display with the proper alignment, a lenticular sheet has the same output function as a parallax barrier [28-30]. For this reason, lenticular sheets suffer from the same drawbacks as parallax barriers, but they do provide the advantage of higher optical efficiency since there are no occluding elements placed above the display. The concept of light field displays based on lenticular sheets is illustrated in Fig. 1.8 [10].

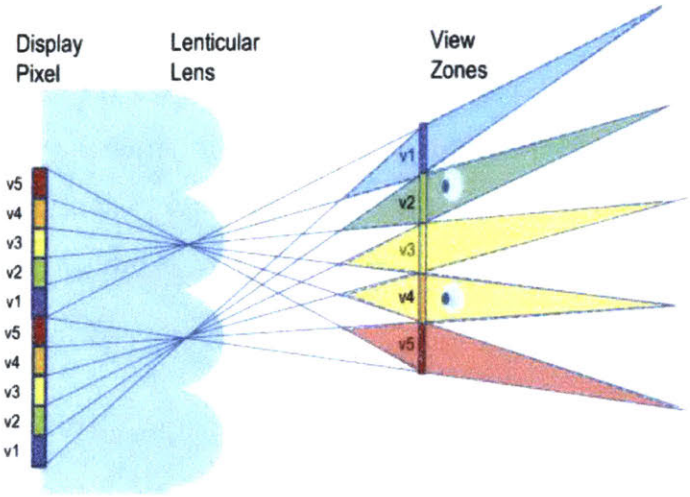

Figure 1.8. Schematic of horizontal parallax only lenticular sheet concept [10].

1.3.3 Integral Imaging

The two display methods discussed above are both one-dimensional technologies and therefore only provide horizontal parallax. Integral imaging is effectively the expansion of the parallax barrier and lenticular sheet concepts into two dimensions using a 2D array of pinholes or spherical lenses, respectively [31-32]. This method derives from a technique develop by Lippmann in 1908 called integral photography

[33]. Integral photography involves the recording of a 3D scene through an array of spherical lenses, behind each of which lies a dedicated individual sensor array or a section of a sensor array so as to capture multiple perspectives of the scene. This image capture mechanism is shown in Fig. 1.9 [32]. The captured sub-images are referred to as elemental images. While the concept of integral photography has been known for over a century, only recent advances in microlens array fabrication and high resolution CMOS imager technology have enabled its realization. An integral imaging display is simply the reciprocal of the imaging system described above, as shown in Fig. 1.9 [32]. In the display configuration, elemental images may be captured from a real scene or computationally generated in order to reproduce the desired virtual scene. Integral imaging provides high quality quasi-continuous parallax in both horizontal and vertical dimensions, but still suffers from low resolution due to the fact that each elemental image must have the same resolution as the desired resolution of the virtual image. High resolution displays therefore become difficult to achieve as the number of elemental images is increased.

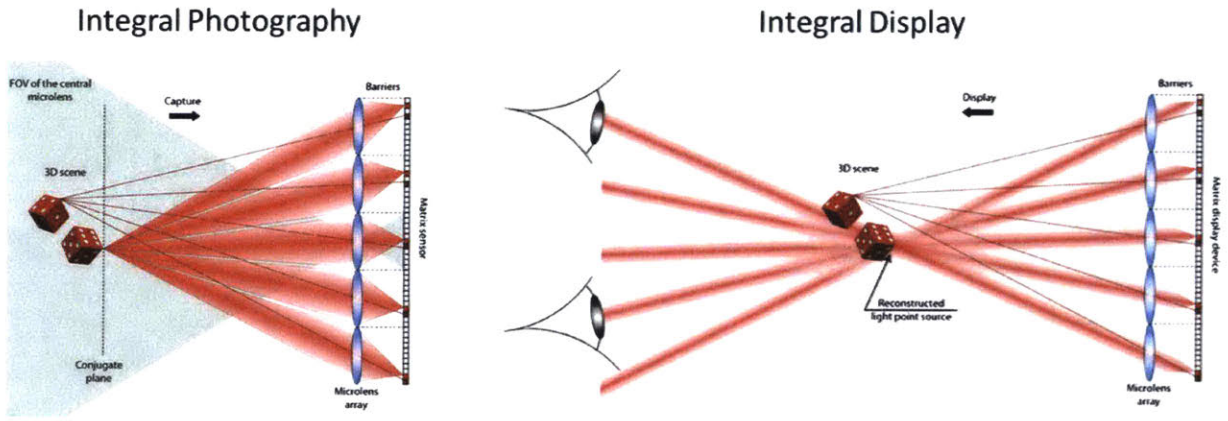

Figure 1.9. Conceptual schematic of integral photography and display [32].

1.3.4 Projection-Based Autostereoscopy

In the last few years, there have also been investigations of generating light fields using arrays of projectors [34-37]. Current projector technologies are capable of emitting light with high directionality, thereby making them suitable for light-field projection. An advantage of projection based methods is the ability to generate virtual objects within a certain image volume in free space in front of the projector array. The projector-based light-field display method is illustrated in Fig. 1.10. The majority of projector-based systems demonstrated to date have been horizontal parallax only (HPO), in which vertical parallax is discarded by means of an asymmetric diffuser. This is done to reduce the size and complexity of the system while also decreasing the amount of data necessary per frame to generate 3D images. This solution may be practical for certain display systems where a viewer is significantly mobile in the horizontal direction but the vertical height from which viewers see the display may not change. One significant disadvantage of HPO systems is that accurate monocular depth cues are discarded along with vertical parallax since angular information in the vertical direction is generated only at the plane of the diffuser. This gives rise to the vergence-accommodation conflict. Specifically, this means that while the viewer's

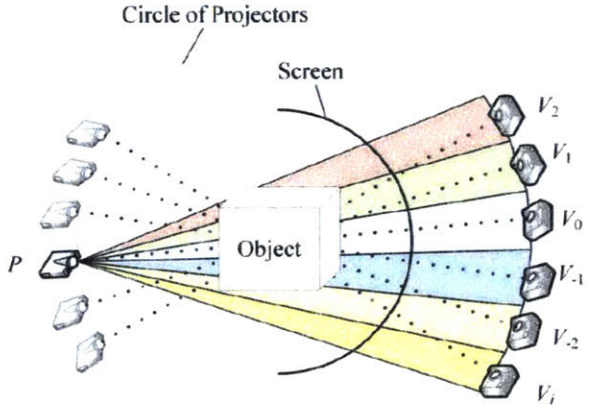

Figure 1.10. Schematic of a horizontal parallax only projector-based autostereoscopic display [34]

eyes may converge to any given point in the 3D image volume, the eyes will individually accommodate only to the plane of the diffuser, thereby resulting in discomfort and eye fatigue which preclude prolonged viewing. It is therefore essential that 2D projection-based methods be developed in the future for the generation of dynamic 3D images with all physiological depth cues.

2 Phased Array Autostereoscopy

The 3D image projection method based on integrated optical phased arrays presented in this work is conceptually similar to the projection based method discussed in Section 1.3.4. As discussed in Section 1.1, it is possible to configure relative phases of elements in a phased array to project arbitrary intensity patterns in the far field. The prospect of utilizing integrated optical phased arrays as a reconfigurable 2D image projector has been suggested, but demonstrated only at infrared wavelengths [38]. Such a device would be especially useful for implementing micro-projectors to be incorporated into mobile devices such as cell phones.

A micro-projector based on integrated optical phased array offers several advantages when compared to its commercial counterparts, such as those based on digital light processing (DLP) and liquid crystal on silicon (LCOS) microdisplay technologies. Both of these are reflection-mode technologies in which pixels may be turned on or off in a grayscale manner. Existing micro-projector technologies also require a lens to project the microdisplay image. Pixels in a DLP system are micro-mirrors which can be tilted towards or away from the projection lens, thereby effectively turning the pixel on or off, respectively [39]. Pixels in an LCOS system are defined by a grid of electrodes patterned in an integrated CMOS circuit to locally tune liquid crystals in an overlying liquid crystal layer to an on or off state [20]. In both systems, optical efficiency inherently decreases when incoming light is discarded by pixels in their off-state. An integrated optical phased array mitigates the issue of optical efficiency seen in existing systems since all incoming light is distributed amongst the antennas. Integrated optical phased arrays are also lens-free projection systems with all optical functionalities implemented on chip, which results in an extremely compact package that can be easily incorporated into mobile devices. Additionally, the ability to fabricate large scale integrated optical phased array

systems with high precision in state of the art 300 mm wafer CMOS foundries will enable low-cost large-scale manufacturing of this technology.

With the emergence of robust and highly accurate large scale integrated photonics fabrication technology, systems of integrated optical phased arrays for projection-based autostereoscopy may now be fabricated. Compared to current projector-based autostereoscopic systems, one based on integrated optical phased arrays offers the immediate advantage of miniaturizing the optical system such that the functionalities of all necessary projectors are incorporated onto a single chip. This results in a single standalone optical device with fully integrated tunable components for 3D image projection without the need for any external bulk optical components such as lenses, thereby readily lending itself to incorporation into mobile devices as a compact glass-free 3D display. Large-scale photonic integration also enables the manufacturing of such systems at a low cost.

2.1 Phased Array Autostereoscopy Concept

This work involves the design, fabrication, and characterization of systems of visible light integrated optical phased arrays for projection-based autostereoscopy. Such a system is specifically comprised of a grid of tiled integrated optical phased array projectors on a single chip, each generating the necessary radiation pattern in its far field for reproducing the light field of the desired virtual 3D object. All phased arrays in the system must be incoherent with respect to each other so that their far fields remain independent. As detailed in a previous section, the far field radiates spherically outward such that points in the far-field radiation pattern represent angular directions. The necessary far-field pattern for a given array is therefore determined by mapping each virtual point in the 3D image volume above the display to an angle in its far field. The extents of the image volume, given a certain display size and virtual object placement along the z-axis defined as the axis normal to the

chip, is determined by the angular extents of the 0th order windows of the phased arrays on the edges of the display, as illustrated in Fig. 2.1. The minimum spatial extent of a voxel is determined by the diffraction limit of a single phased array, which in one dimension is given by

$$\theta_d \approx 0.886 \frac{\lambda}{Nd} \tag{2.1}$$

where θ_d is specifically the full-width half-maximum of the far-field spot generated by a uniform phase and amplitude near field distribution, λ is the wavelength, N is the number of antenna elements and d is the element spacing, with Nd defining the aperture of the phased array [8]. The minimum size of a voxel is therefore given by the width of the diffraction limited spot formed at the radial distance from the center of the phased array that is farthest from the voxel, as shown in Fig. 2.1. θ_d in Equation 2.1 is also the minimum angular separation between two resolvable spots in the far field of a phased array. Therefore, the number of phased arrays of a given size needed to project a virtual point source in space within a specified field of view θ_{FOV} for providing continuous parallax in one dimension is

$$N_{PA} = \frac{\theta_{FOV}}{\theta_d} \tag{2.2}$$

The resolution of the virtual image is also determined by θ_d, which specifically determines the minimum separation between adjacent voxels given a certain radial distance from the center of the farthest array. A conceptual depiction of the arrangement of voxels in a 2D image volume as bound by the diffraction limit of a phased array and given a 1D grid of phased arrays is shown in Fig. 2.1. This set of voxels forms the basis onto which virtual images may be encoded.

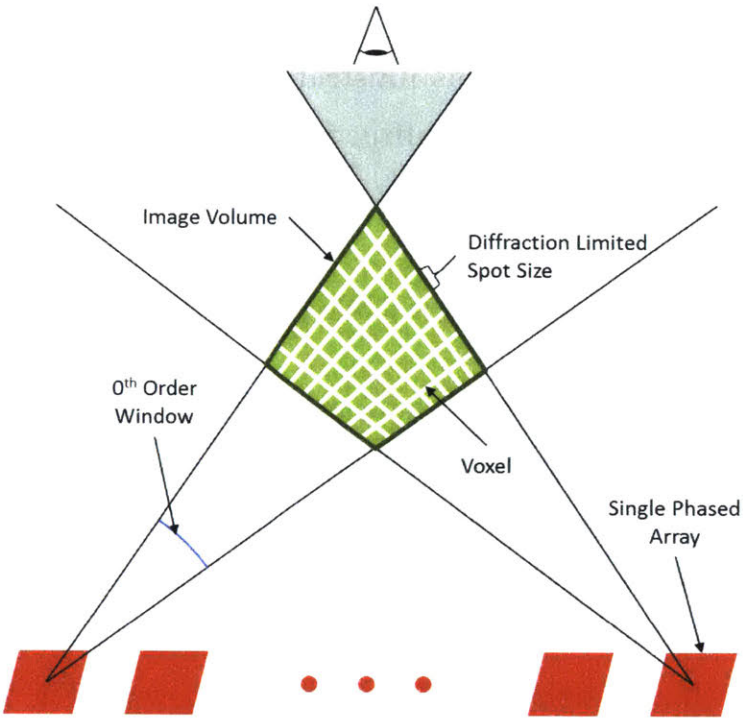

Figure 2.1 Schematic of the definition of the image volume and voxel grid in a phased-array-based autostereoscopic image projection system.

2.2 Phased Array Synthesis

As discussed in section 2.1, a series of independent phased arrays may be configured such that they each project a portion of the information that comprises a 3D object. In this system, each phased array projects light through every point in a 3D object at an angle corresponding to the geometric angle at which the 3D object lies with respect to the center of the phased array, as shown in Fig. 2.2. If multiple phased arrays are densely tiled such that each point in the 3D object is illuminated from a range of angles, near-continuous parallax and depth may be observed in the virtual 3D scene.

A demonstration of a tiled visible light optical phased array system using the phased array architecture detailed in the previous section is presented in this work. Due to limitations on the available reticle space in the 300 mm wafer fabrication process, the proof of concept was designed to exhibit only horizontal parallax, for

which only a one-dimensional array of phased arrays is needed. An asymmetric diffuser is then placed at the plane of the virtual image to discard vertical parallax, as seen in the schematic of the horizontal parallax characterization setup shown in Fig. 2.2. In the system presented in this work, a one-dimensional array of sixteen 32×32 emitter visible light integrated optical phased arrays is used to project the necessary angular information for a virtual 3D scene. The 3D object chosen for this proof of concept was a pyramid, viewed from an azimuthal perspective at an angle with respect to the zenith of the pyramid as shown in Fig. 2.2. A more complex 3D

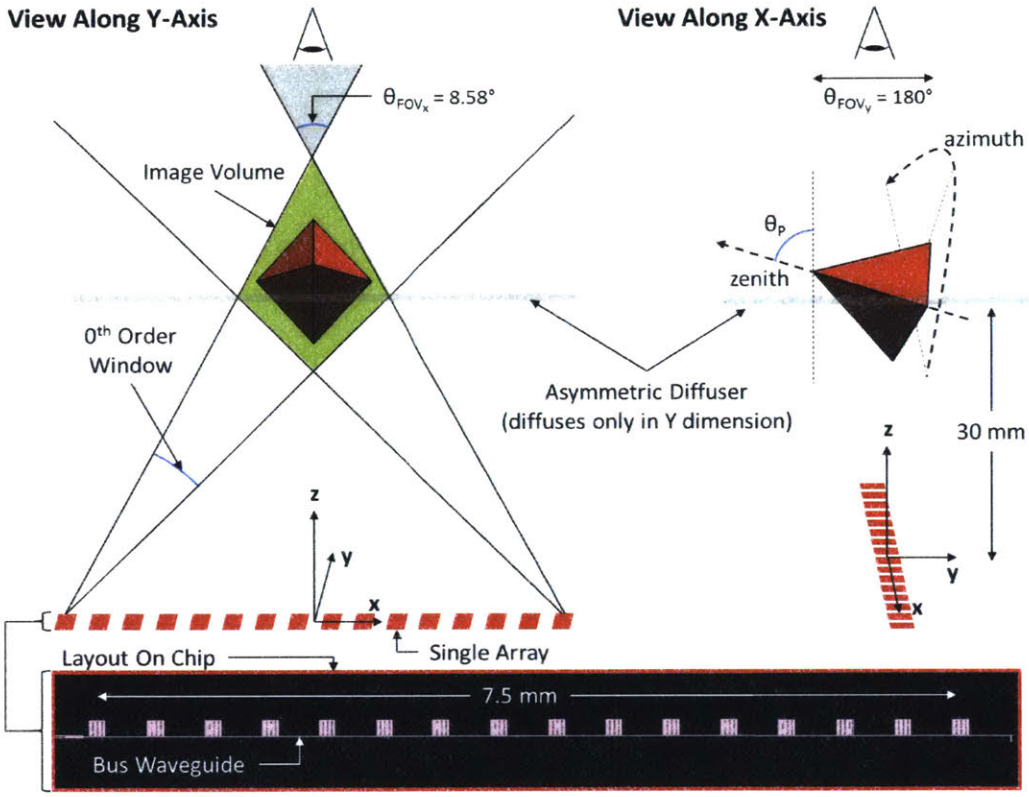

Figure 2.2. Views along the x- and y-axes of the horizontal parallax only image projection system. The placement and orientation of the virtual object in the image volume as well as those of the asymmetric diffuser for discarding vertical parallax are shown. The image highlighted in red shows the layout of the image projection system with 16 equally spaced phased arrays, each encoded with the appropriate phase distribution for projecting the necessary angular information for the virtual image from its respective position.

object is difficult to generate with high resolution using only 32×32 emitter phased arrays. The size and position of the 3D object was chosen such that it would fit within a single order window of the phased array while allowing an appreciable field of view (FOV). The system presented here, the parameters for which are detailed in Fig. 2.2, provided an FOV of 8.58° with a phased array spacing of 500 μm for a virtual image of a pyramid placed 30 mm above the chip. A schematic of the layout of the system is also shown in Fig. 2.2.

The necessary far-field intensity distribution of each phased array in the projection system was configured to contain the angular information to illuminate every visible point in the 3D object as if the source of the illumination originated from the center of that phased array. To determine the target far-field image to be used as the input to the GS algorithm for each phased array, the desired 3D object, a pyramid in this case, was first discretized into points in a 3D space and represented as voxels (effectively 3D pixels) in a 3D matrix in MATLAB. A visualization of this 3D matrix for the chosen virtual object is shown in Fig. 2.3. Each point represents a position in 3D space and is encoded with an illumination intensity in relative power units between 0 and 1. It should be noted that only the surfaces of 3D objects are seen by the viewer. Therefore, only points on the surfaces of the object must be represented in the 3D space. In this case, only two faces of the pyramid are visible to the viewer from any position in the field of view so only the points defining these surfaces were encoded into the virtual 3D space. While the object is encoded in a physical 3D space represented with Cartesian coordinates, the far field of a phased array is an angular space and the input to the GS algorithm must be expressed in the (u,v) space defined in Section 1.1. The Cartesian 3D object data is translated onto the 2D (u,v) space by converting the matrix to spherical coordinates and discarding the radial distance r. This then yields a list of coordinates, each representing a specific polar and azimuthal angle where the origin is the center of the phased array and containing a parameter defining the intensity. It should be noted that the initial 3D object must be pre-processed to ensure that no two points on the surfaces expressed in 3D Cartesian

coordinates lie along the same radial line. Alternatively, if two points in the 3D object do lie along the same radial line, one may later be discarded by determining which point is closest to the viewer. The list of (u,v) points defining the 3D object are then interpolated onto a rectangular point grid in (u,v) space using the *scatteredInterpolant* function in MATLAB to generate an array representing the desired far-field intensity distribution for passing into the GS algorithm.

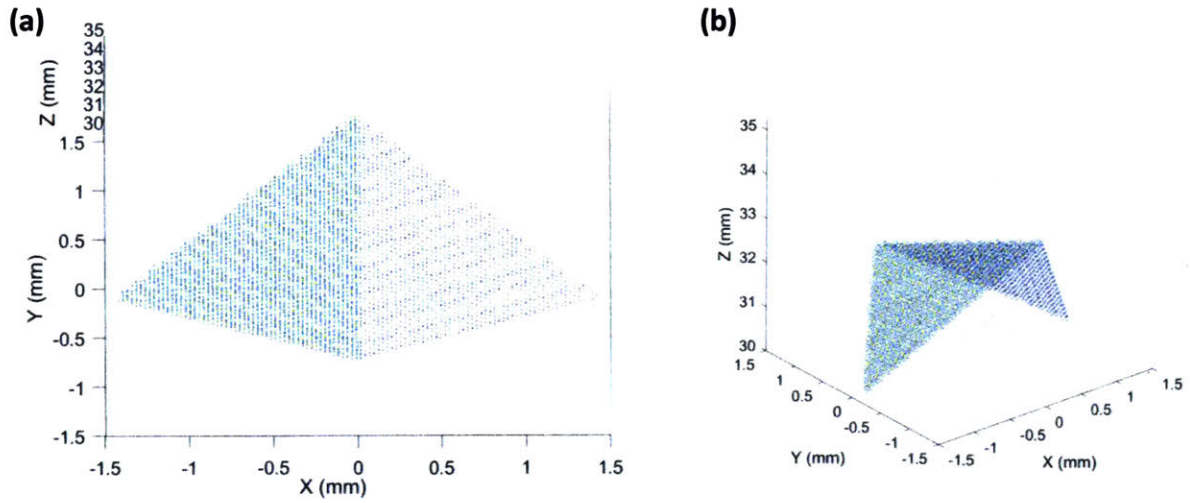

Figure 2.3. Visualization of the initial Cartesian 3D voxel encoding of the surface of the virtual pyramid visible to the viewer. Two perspectives of this voxel space are given to provide greater intuition of the voxel encoding.

For phased arrays that are far from the center of the projection system, it is possible that the necessary angular information required from these arrays may not lie entirely in their 0th order windows, as shown in Fig. 2.4(a). To account for this in the calculation of the target far-field intensity distribution, the extents of the virtual object in (u,v) space are calculated after the 3D-to-2D coordinate conversion step detailed above. The coordinate list is then shifted by the amount corresponding to the negative of the distance of the center of the object from the origin along both dimensions such that the center of the object lies at $(u,v) = (0,0)$. This distance is

$$u, v_{center} = \frac{u, v_{max} - u, v_{min}}{2} \tag{2.3}$$

where u,v_{max} *and* u,v_{min} represent the maximum and minimum extents of the virtual object in (u,v) space. The interpolation of virtual object points onto a square grid matrix is then carried out as in the steps outlined earlier. The interpolated image is then circularly shifted in both dimensions by u,v_{center} using the *circshift* function in MATLAB to return the virtual object to its original position while ensuring that all necessary far-field information is included in a single order before passing the resulting intensity distribution to the GS algorithm. The target far-field patterns after interpolation and the associated calculated far-field radiation patterns of five of the phased arrays in the 16-array system are shown in Fig. 2.4(b).

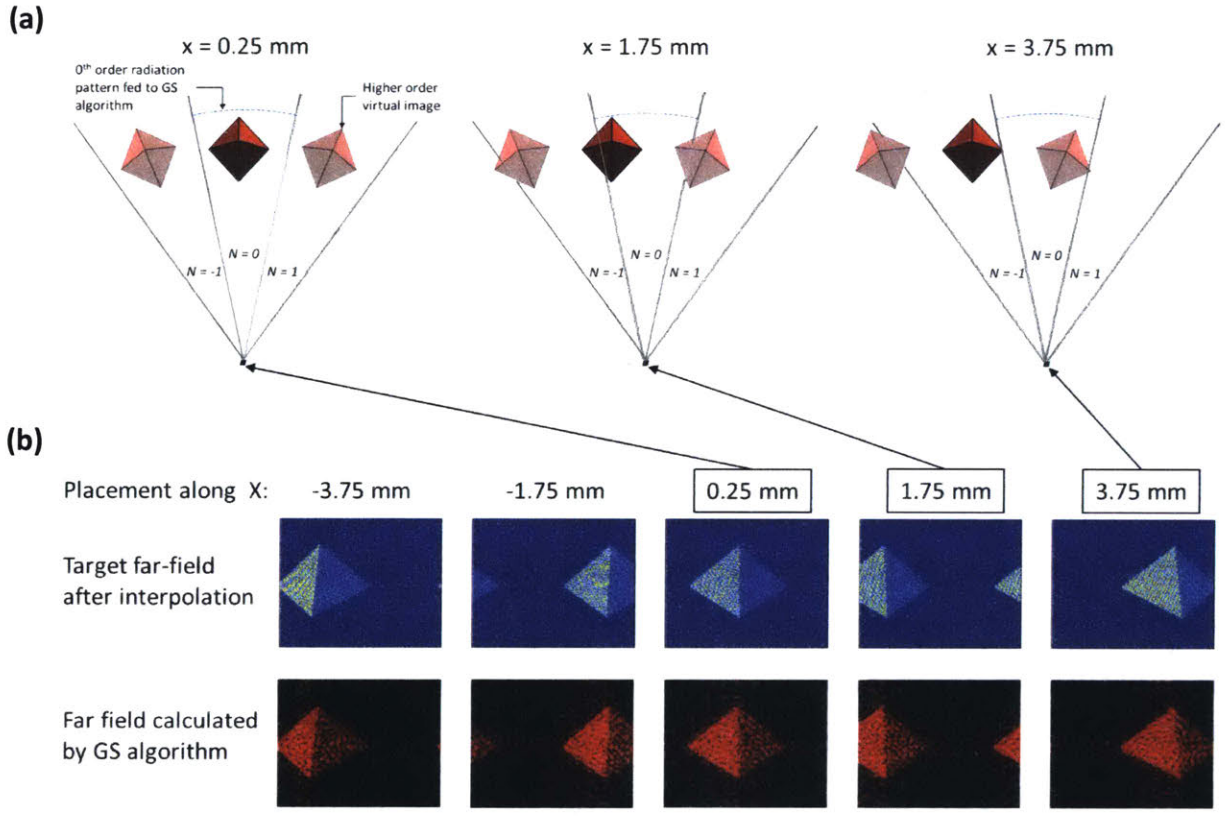

Figure 2.4. (a) Locations of interference orders N with respect to the virtual image location (not to scale) illustrating the need for centering the necessary radiation pattern within a diffraction order prior to interpolation and circularly shifting the matrix containing the resulting pattern by the appropriate amount before feeding it to the GS algorithm. (b) Target and calculated far fields are shown for five of the phased arrays in the display for a virtual image placement of 30 mm in z.

2.3 Passive Phased Array Design

As mentioned in Section 1.2, 2D phased arrays with individual antenna phase control must utilize cascaded light distribution in at least one dimension. The 64×64 unit cell passive silicon photonic phased array discussed in Section I, which was encoded with the necessary phase distribution for projecting the MIT logo in the far field, utilized cascaded light distribution along both dimensions [5]. Good agreement between simulated and measured far-field radiation patterns were observed in these arrays. 2D cascaded light distribution allows for full control of phase within the unit cell, which isolates it from phase errors that may occur in the light distribution system, as may be the case for a tree structure which has a multiplicative effect on phase errors as they propagate through multiple splitting stages. Phase errors due to fabrication errors in the bus waveguides of cascaded distribution systems may occur, but these result mostly in the addition of a linear phase gradient to the phase distribution and slightly change the emission angle of the far-field radiation pattern. Given the advantages outlined above, a 2D cascaded light distribution system was chosen to implement the 2D visible light phased arrays for projecting the arbitrary far-field patterns for the autostereoscopic image projection system discussed in the previous section.

Phased arrays and their associated components discussed in this section were all designed for the visible wavelength of 635 nm in a 200 nm thick silicon nitride layer with silicon dioxide cladding. Phased array unit cells were similar to those used in [5], consisting of a directional coupler to tap light from a bus waveguide and a short grating section to couple light into free space. A diagram of the designed unit cell and its far field are shown in Fig. 2.5. The unit cell pitch is 4 μm in both directions, which results in an approximately 9.1° 0^{th} order window. Unfortunately, this pitch was achieved at the expense of antenna emission efficiency. Specifically, the bend radius of the waveguide in the unit cell is significantly below the critical bend radius for the chosen waveguide geometry, thereby resulting in bend losses. A slight offset between the directional coupling and curve regions of the unit cell waveguide, shown in Fig.

2.5(a), is applied to compensate for mode mismatch between the two regions. Also the grating is not sufficiently strong for coupling all incoming light to free space. Despite these drawbacks, sacrificing efficiency for minimizing pitch was necessary because a lower pitch yields a larger 0^{th} order window, and therefore a larger field of view for autostereoscopic 3D image projection applications. Future designs may incorporate a thicker silicon nitride layer or a dual-nitride layer waveguide to increase the confinement of light in the waveguide and in turn increase the emission efficiency for the same unit cell pitch.

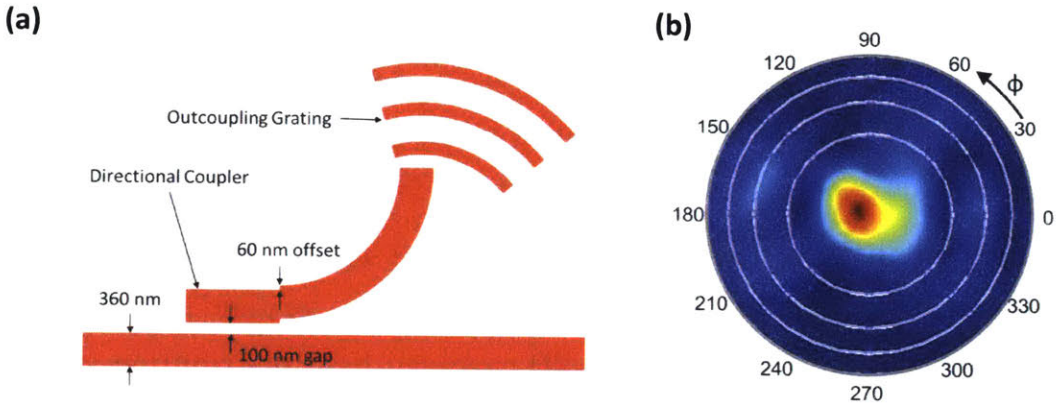

Figure 2.5. (a) Schematic of the 4 μm unit cell utilized in the passive 2D phased array architecture and its (b) far-field radiation pattern.

32×32 emitter passive phased arrays were fabricated with the light distribution system and unit cell design discussed above. A schematic of the phased array is shown in Fig. 2.6(a). Light from a 635-nm fiber-coupled diode laser is edge-coupled into a main bus waveguide. Light is then coupled to periodically spaced row bus waveguides via a series of directional couplers. The length of the directional couplers is increased along the length of the main bus waveguide to deliver an equal amount of light to each row. Light in each row bus waveguide is coupled to periodically spaced emitters with increasing directional couplers lengths along the row in the same manner as in the main bus waveguide to ensure a uniform near-field emission profile. A plot of coupling percentage versus coupling length is also shown in Fig. 2.6(b).

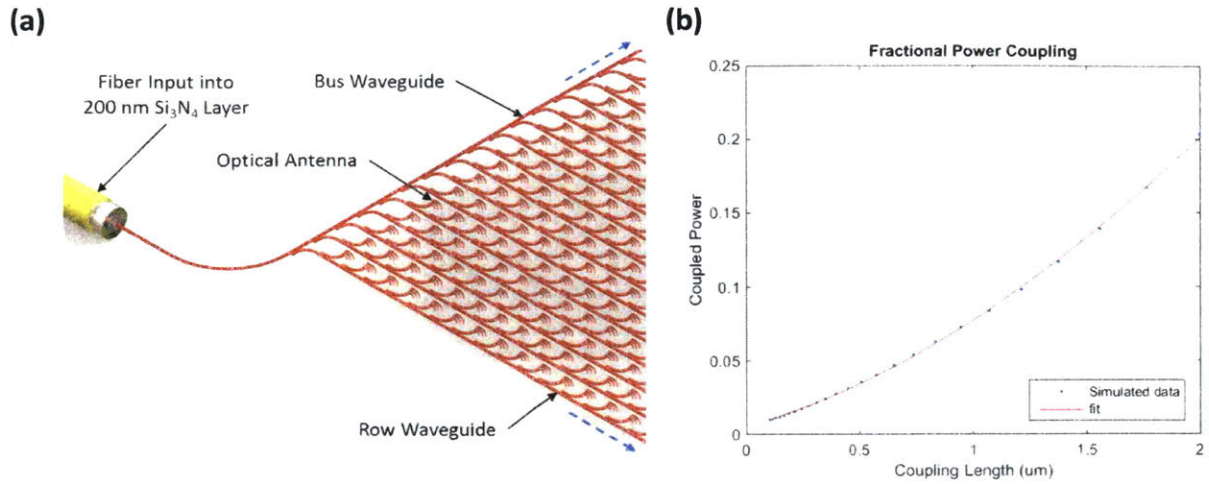

Figure 2.6. (a) Schematic of passive phased array architecture. (b) Coupling fraction vs. length for the directional coupler used in the cascaded light distribution system.

Unlike the unit cell in [5], unit cells designed in this work did not incorporate a phase modulation section after the directional coupling region since this would significantly increase emitter pitch. Instead, relative phase was encoded into each unit cell by shifting its position along the row bus waveguide by an amount equivalent to the desired phase shift with respect to its default position according to a 4 μm pitch grid. The necessary shift in position for a given desired phase shift is determined by the effective index of the waveguide mode as

$$L_{shift} = \frac{\varphi\lambda}{2\pi n_{eff}} \tag{2.4}$$

where φ is the desired phase shift, λ is wavelength, and n_{eff} is the effective index. The unit cell may be displaced by $\pm\frac{\lambda}{2n_{eff}}$, which is equivalent to a phase shift of $\pm\pi$, to achieve full 2π phase tuning. This physical displacement is subwavelength and of significantly lower magnitude than the unit cell pitch. The noise in the far-field radiation pattern resulting from these spatial offsets is therefore negligible. A close-up of a section of the layout of one the designed phased arrays, shown in Fig. 2.7, illustrates the phase encoding mechanism.

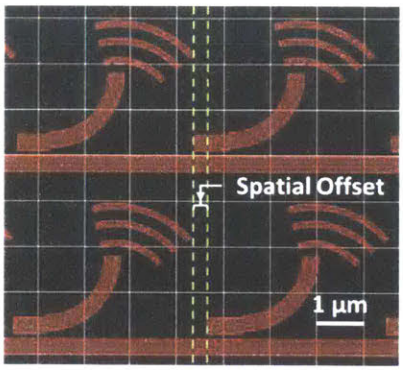

Figure 2.7. Close-up of the layout of one of the passive phased arrays demonstrating the phase encoding mechanism based on physical unit cell offsets.

When implementing the phase encoding mechanism described above, phase distortions resulting from the effective index of the mode in the directional coupler region differing from that in single waveguide sections must be taken into account. This phase deviation, simulated using FDTD for different coupling lengths, is plotted in Fig. 8. For each unit cell, the phase distortion caused by the directional coupler is compensated by shifting the unit cell by a distance that negates the phase deviation in addition to the distance necessary for the assigned relative phase shift.

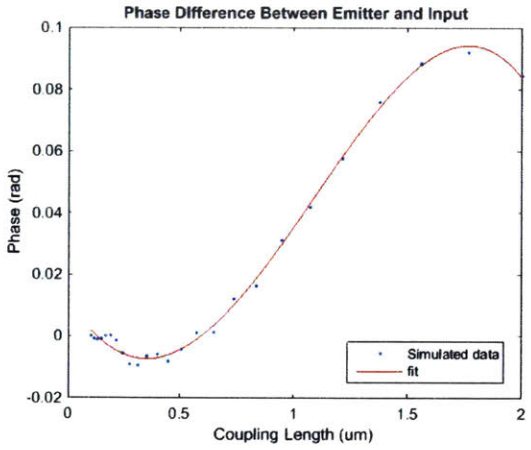

Figure 2.8. Plot of the phase deviation in a unit cell versus the length of the directional coupler.

The near field of a 32×32 phased array is shown in Fig. 2.9(a). A fairly uniform near-field emission profile is observed. This phased array was encoded with the phase distribution necessary for projection an angular perspective of a pyramid, as shown in Fig. 2.9(b). One face of the pyramid was shaded to demonstrate the ability to project images with varying intensity distributions while tuning only the phase of emitters in the phased array. The necessary phase distribution for projecting this image was calculated using the GS algorithm. It can be seen that the far-field pattern produced by the GS algorithm does not perfectly converge to the target far field, but is still a very close approximation. This deviation from the target far-field is largely due to the finite emitter count and the lack of antenna amplitude control, both of which decrease the number of available degrees of freedom that may be varied in order to achieve the desired far-field pattern.

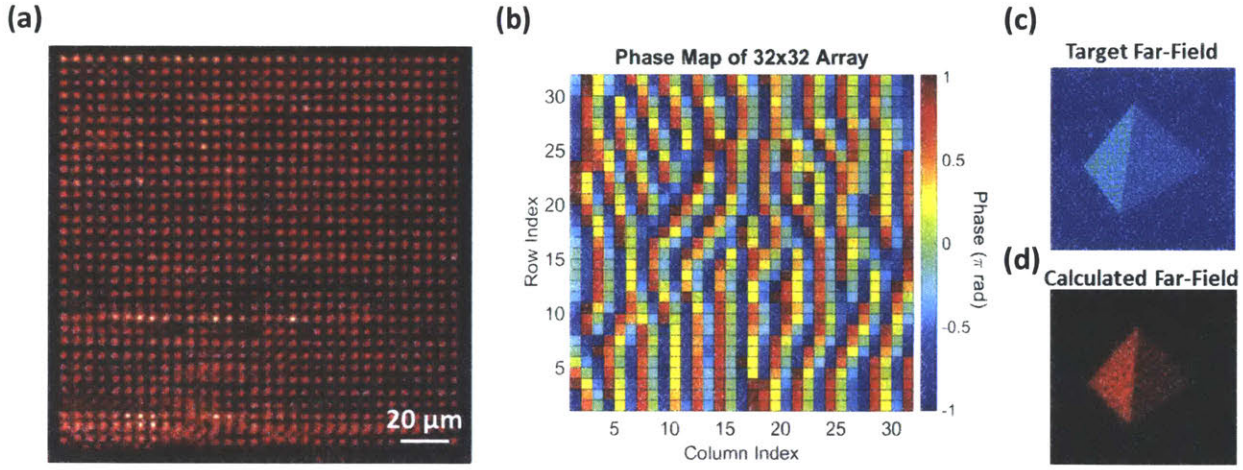

Figure 2.9. (a) Measured near field of a 32×32 passive phased array. (b) Antenna phase distribution necessary for generating the far-field (d) calculated using the GS algorithm with the image (c) as the input.

Measured far-fields of three of the phased arrays in the 16-array image projection system appropriately encoded to project the necessary radiation pattern with respect to their positions on the display are shown in Fig. 2.10. Higher orders are seen in measured data as in simulations. The measured far-field radiation patterns show

very good agreement with simulations, thereby showcasing the robustness of the fabrication process used to implement these phased arrays.

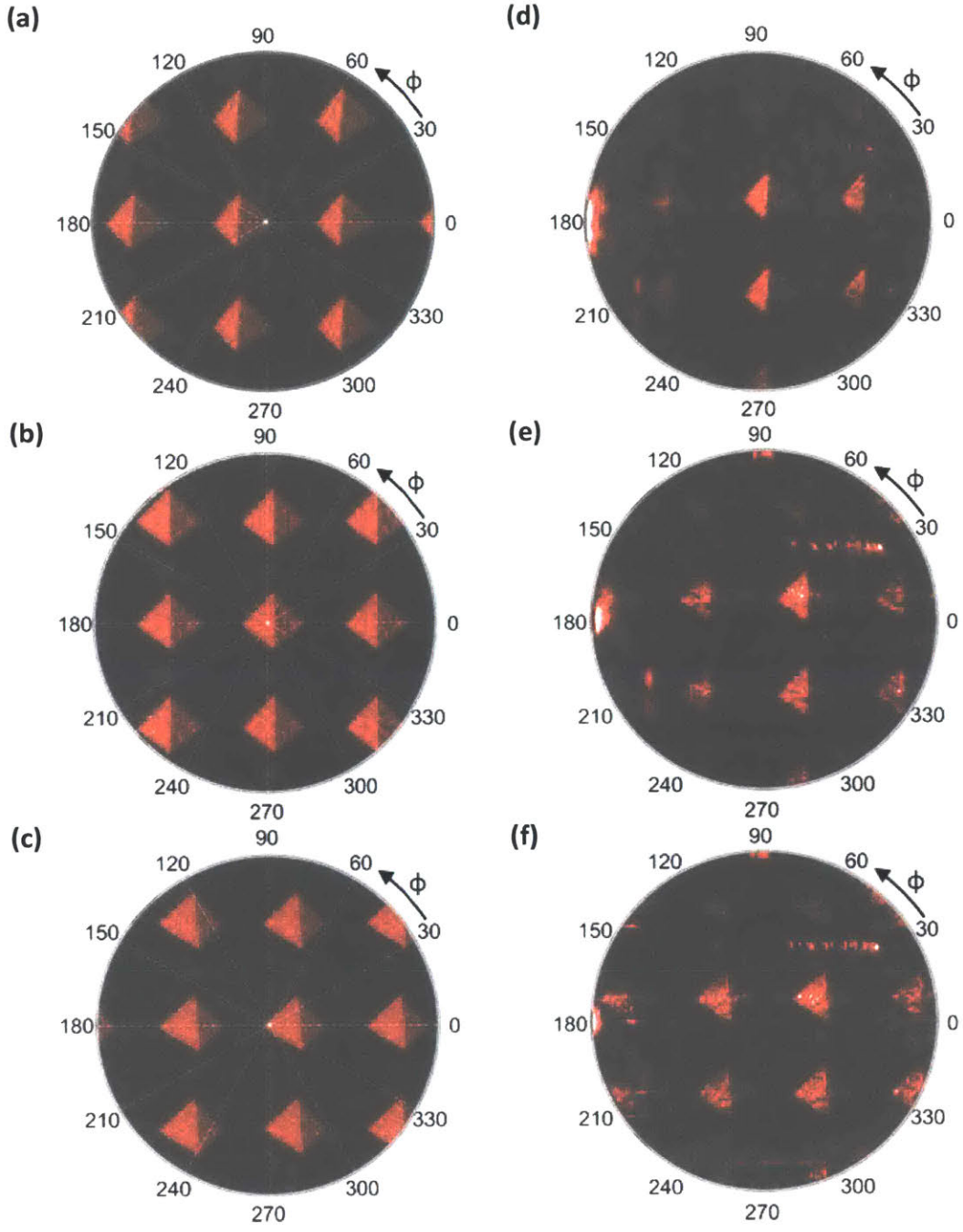

Figure 2.10. (a-c) Simulated and (d-f) measured far fields of three of the 32×32 phased arrays in the 16 phased array horizontal parallax only autostereoscopic image projection system.

2.4 Demonstration of Horizontal Parallax

The image formed after propagation of the emitted light through the asymmetric diffuser was relatively small. A lens was placed immediately after the asymmetric diffuser to slightly magnify the virtual image to enable viewers to more readily observe the parallax. The limited numerical aperture of the lens also filtered out some scattering artifacts from the diffuser surface. Images of the virtual image taken from three different angles to demonstrate horizontal parallax are shown in Fig. 2.11. As seen in these images, parallax may be observed in the higher order virtual images as well. Higher order virtual images have independent FOVs in which the virtual object is rotated with respect to the 0^{th} order image by angle at which the specific higher far-field order is formed. This can also be observed by noting that from any given viewpoint, higher order virtual objects will appear rotated to different extents compared to the 0^{th} order.

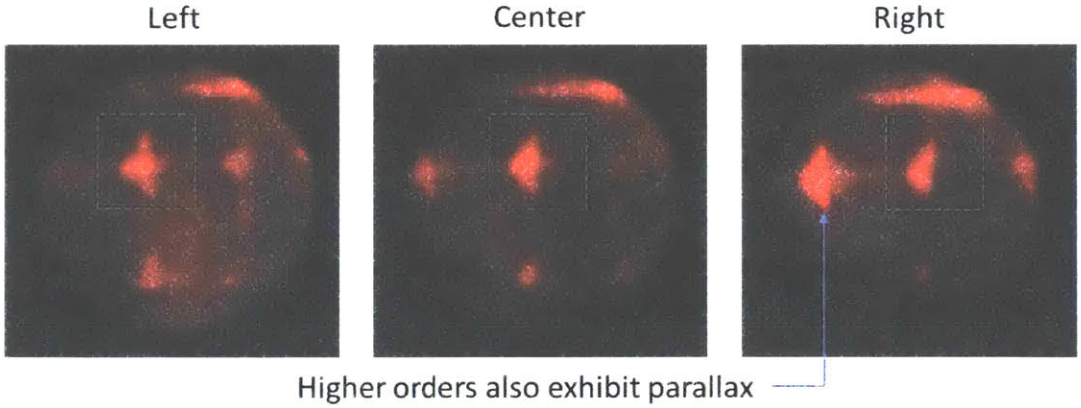

Figure 2.11. Camera images of autostereoscopic horizontal parallax only image viewed from left, right, and center perspectives.

3 Large Aperture Visible Light Phased Arrays

As discussed in previous sections, integrated visible light phased arrays may be used as compact, low-power and low cost solutions for a range of applications including autostereoscopic 3D displays, neuronal targeting for optogenetics, and fluorescence-based bioimaging. In order to implement commercially viable phased array systems for these applications, large-scale phased arrays with highly accurate fabrication for low noise radiation pattern generation must be demonstrated. To this end, large-aperture 1D uniform phase and amplitude visible light phased arrays using waveguide grating antennas for red, green, and blue wavelengths were demonstrated. The design, fabrication, and characterization of these devices is discussed in this section. The work presented in this section was a collaborative effort between Christopher Poulton, Matthew Byrd, and Manan Raval (author).

3.1 Waveguide Grating Antenna Design

A waveguide grating antenna consists of a waveguide with periodic perturbations to coherently couple guided light to free space. The strength of the perturbations along the waveguide will determine the length of the antenna for a given target signal emission percentage. The extent of the antenna dimension of a phased array comprised of waveguide grating antennas is therefore defined by the length of the antenna. The extent of the other dimension, referred to henceforth as the array dimension, is determined by the number of antennas in the phased array multiplied by the antenna spacing. Architectures using waveguide grating antennas generally only afford 1D phase control, but wavelength tuning is often used to implement

steering in the remaining dimension [6]. Despite this limitation, waveguide grating antennas enable much lower antenna pitch than the unit-cell-based design presented in Section 2.3. Both a cascaded or tree distribution system, discussed in Section 1.2, may be utilized to deliver an equal amount of light to each antenna.

While phased arrays based on waveguide grating antennas have been previously demonstrated [3,6,7], the present work will focus on their design and fabrication in silicon nitride, primarily for operation in the visible spectrum. A waveguide grating antenna may nominally be designed by introducing periodic variations in the width of a waveguide, as shown in Fig. 3.1(a). Specifically, perturbations are sections of the waveguide in which the width is decreased with respect to the initial waveguide width. The perturbation will henceforth be quantified as the decrease in the lateral extent of the waveguide on one side, as shown in Fig. 3.1. The emission is defined as the fraction of light emitted per unit length, measured in dB/μm. The perturbation period is chosen to impose a certain emission direction based on the Bragg condition, given as

$$-\frac{n_c}{\lambda}\sin\theta + \frac{n_{eff}}{\lambda} = \frac{1}{\Lambda} \tag{3.1}$$

where θ is the angle of emission, n_c is the index of the oxide cladding, n_{eff} is the effective index of the waveguide, λ is the wavelength, and Λ is the period of the grating [40].

In its simplest implementation, a waveguide grating antenna is designed with a constant perturbation, which results in an exponential decrease in the emission intensity along the antenna [7]. If the perturbation period is chosen to be the equivalent of a 2π phase shift or a single wavelength, higher orders of the grating emission will lie in the plane of the waveguide, resulting in significant back-reflections. This issue may be mitigated by adjusting the perturbation period such that it is equivalent to a phase shift slightly greater than or less than 2π, which results in the emission being at an angle with respect to the normal. Alternatively,

the perturbation strength may be increased along the length of the antenna to achieve a uniform near-field emission profile. Since the perturbation strength depends on the width of the perturbed region, the perturbation pitch must also be increased along the length of the antenna to compensate for the decrease in effective index with waveguide width and maintain the same phase accumulation in each period. An additional benefit afforded by increasing perturbation strength along the antenna is the breaking of forward-backward symmetry in the grating. Specifically, coupling into the backwards propagating mode is greatly reduced since this mode couples to a much narrower output beam than does the forward propagating mode [41]. A schematic illustrating the difference between the two designs is given in Fig. 3.1. In a design with varied perturbation strength, each grating period must be adjusted such that its corresponding phase delay is equal to 2π for upward emission or another specific phase delay chosen for emission at a given angle, as illustrated in Fig. 3.1(b). In the presented work, this was done by keeping the length of the full-width waveguide region in each grating period constant while altering the length of the perturbed region to achieve the necessary phase delay.

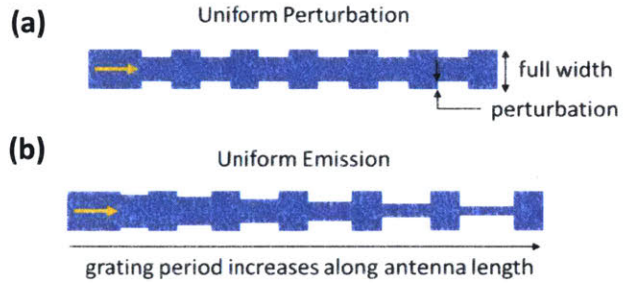

Figure 3.1. Conceptual schematic of (a) uniform perturbation and (b) uniform emission waveguide grating antennas.

Waveguide grating antennas with both constant perturbation strength and increasing perturbation strength for uniform emission were designed for red, green, and blue wavelengths of 635 nm, 532 nm, and 445 nm, respectively. The fabrication process used in this work includes a 200 nm thick silicon nitride layer, thereby

limiting the waveguide height for each wavelength to this value. While a single mode waveguide geometry may be achieved for 635 nm and 532 nm, a TE01 mode arises for 445 nm with this layer thickness.

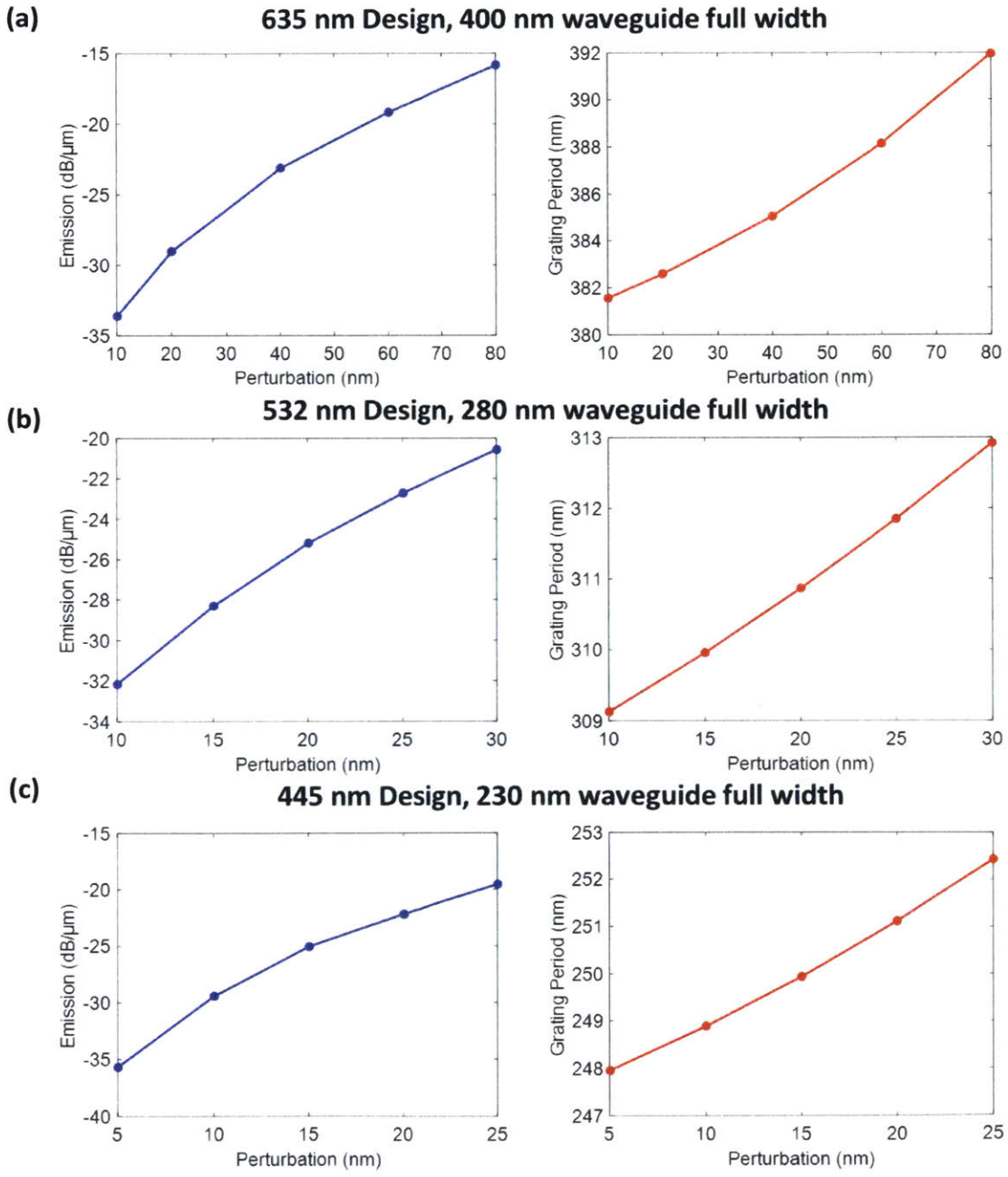

Figure 3.2. Plots of emission and grating preiod versus perturbation (a decrease in waveguide width) for (a) red, (b) green, and (c) blue wavelengths.

3.2 MMI Splitter Trees

A tree comprised of multiple stages of 1×2 multi-mode interference (MMI) 3-dB splitters was used to uniformly distribute the input signal to the array of antennas with uniform phase. In an MMI splitter, light entering a wide multi-mode waveguide region via a narrower input waveguide is reimaged onto two identical output waveguides. While the input and output waveguides need not be single-mode, the incoming signal must ideally be limited to only the fundamental mode, which can be done via an adiabatic taper originating from a single-mode waveguide. The dimensions of the multi-mode waveguide must be engineered such that the higher order modes excited in this region interfere to image the input symmetrically at the output. While the length of the multi-mode region is approximately $L = \frac{3\pi}{8\Delta\beta}$, where $\Delta\beta$ is the difference in the effective index of the first and second (symmetric and asymmetric) modes of the output [42], MMIs for each wavelength were rigorously simulated using FDTD and EME software to determine the ideal dimensions. Simulations and design for MMIs were carried out by Matthew Byrd. The dimensions and simulation results for MMIs designed for red, green, and blue wavelengths are shown in Fig. 3.3. High transmission efficiency is achieved in the MMIs designed for each of the three wavelengths.

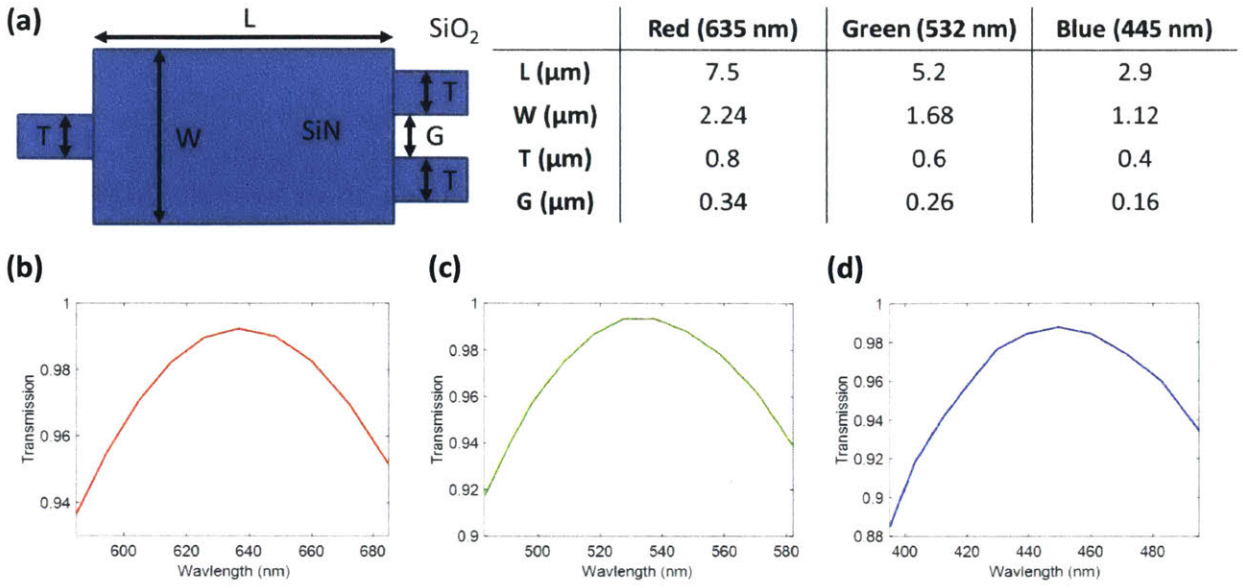

	Red (635 nm)	Green (532 nm)	Blue (445 nm)
L (μm)	7.5	5.2	2.9
W (μm)	2.24	1.68	1.12
T (μm)	0.8	0.6	0.4
G (μm)	0.34	0.26	0.16

Figure 3.3. (a) MMI Schematic with a table of optimized parameters values for designs for the three specified wavelengths. (b-d) Simulated transmission efficiency spectra for the three MMI designs.

3.3 Experimental Data

The measured near and far fields of the red wavelength phased arrays are shown in Fig. 3.4. Full characterization of large-aperture phased arrays was carried out by Christopher Poulton. Both phased arrays were comprised of uniform perturbation antennas arrayed with 2 μm pitch. Uniform amplitude distribution in the array dimension as well as an exponentially decreasing emission profile along the antenna dimension as expected from a uniform perturbation antenna are observed in the near field. Fig. 3.4(a) also shows CMOS camera images of the near-diffraction limited far-field spots generated by both phased arrays. Finally, Fig. 3.4(b) shows an optical image the far-field projected onto a white card. Five of the seven expected interference orders are seen in this image while the two orders furthest from the normal were not captured by the card.

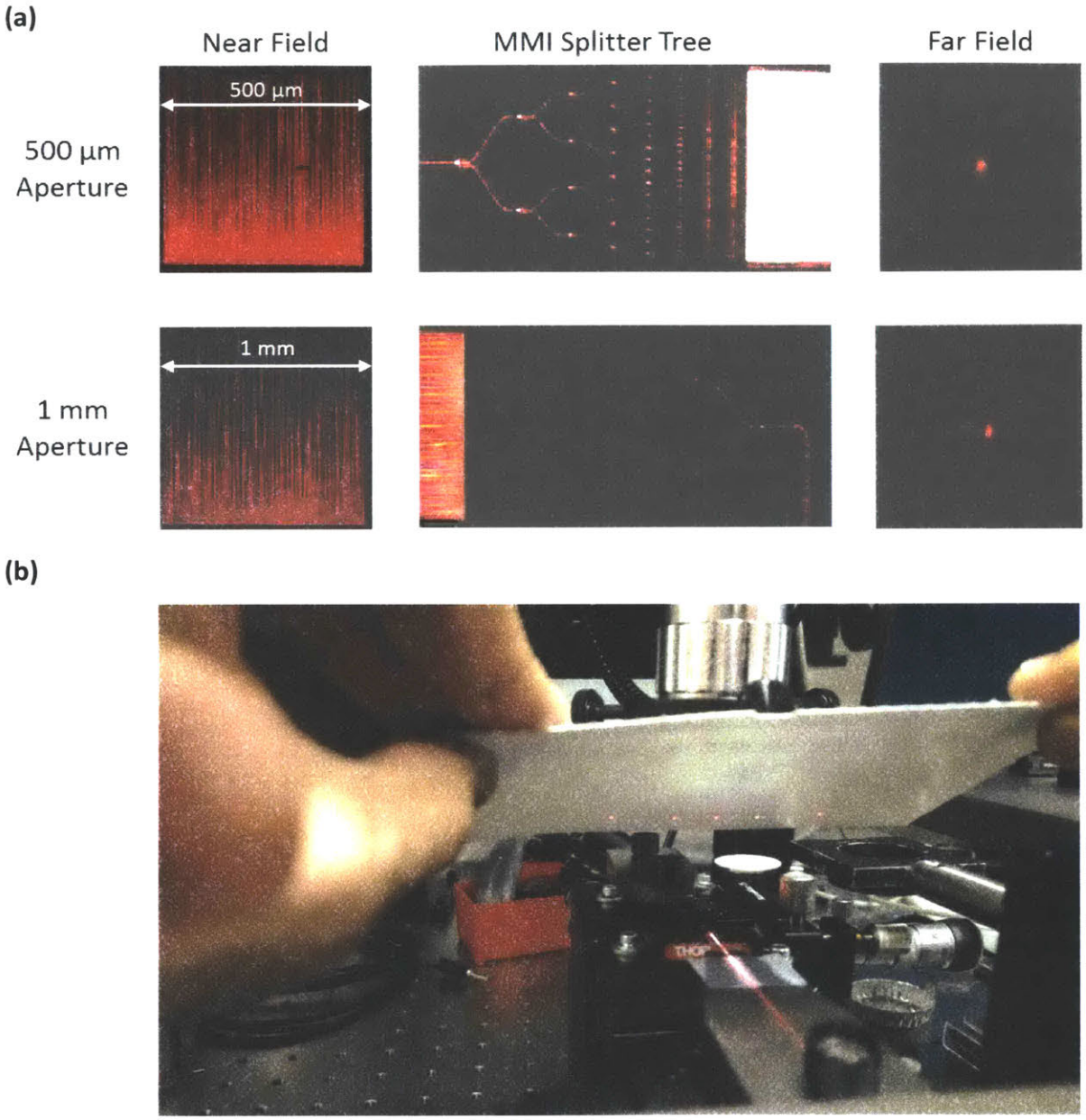

Figure 3.4. (a) Measured near fields and far fields as well as optical micrographs of the MMI splitter tree sections of 500×500 μm^2 and 1×1 mm^2 aperture red (635 nm) phased arrays. (b) Image of the far-field projected onto a card placed above the array.

We were unable to fully characterize the far-field spot of the 1×1 mm^2 aperture phased array primarily due to wavelength instabilities in the diode laser used in the characterization setup, but the angular extents of the far-field spot of the 500×500 μm^2 aperture phased array were accurately measured. Fig. 3.5 shows a surface plot

of the far-field spot of the 500×500 μm² aperture phased array as well as 2D plots of the beam profile along the antenna and array dimensions. The measured spot has a FWHM of 0.064° × 0.074° as compared to the diffraction limited spot size of 0.063° × 0.063°. A side-lobe suppression of 12.7 dB in the antenna dimension and 8.7 dB in the array dimension were observed. The increased spot-size in the antenna dimension is due to the non-uniform emission profile of the constant-perturbation antennas used in this design. Also, a significant deviation from the theoretical side-lobe amplitudes in the array dimension are most likely a result of cascaded phase noise in the splitter tree, which may occur since fabrication errors become more pronounced at visible wavelengths due to higher optical confinement in the silicon nitride.

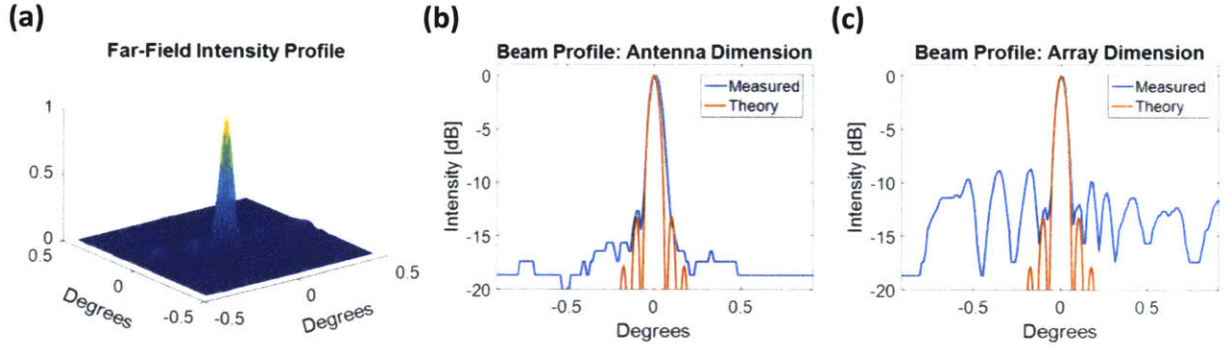

Figure 3.5. (a) Surface plot of far-field intensity profile of 500×500 μm² aperture phased array. 2D plots of the beam profile along the (b) antenna and (c) array dimensions.

We were not able to sufficiently measure the far fields of green arrays because of insufficient edge coupling efficiency onto the chip and of blue phased arrays because of high absorption in the silicon nitride layer. More efficient inverse taper edge couplers and fiber grating couplers for 532 nm will be designed in the near future to enable low noise measurements of the green phased arrays. Also, PECVD or LPCVD deposition recipes may be developed for low-loss silicon nitride at blue wavelengths [43-44]. This would enable the realization of blue light integrated optical phased arrays in the near future.

3.4 Unidirectional Antenna Design

The antenna design discussed in the previous section was vertically symmetric, meaning that half the emitted power is emitted downward and largely absorbed by the substrate. To lower the power consumption of potential optical phased array devices, it is desirable to design antennas with high upward directionality so as to utilize all incoming light. An antenna may be design for unidirectional emission if its vertical symmetry is broken [45-46]. Specifically, this is done by designing a grating in which there are two scatter points in a single period that are separated by a phase difference equivalent to $\lambda/4$ in both horizontal and vertical directions, as shown in Fig. 3.6. This results in destructive interference in the downward emission and constructive interference in the upward emission. While unidirectional gratings have been demonstrated using this concept, previous work has focused primarily on fiber coupling gratings [46-47]. This work demonstrates this concept for waveguide grating antennas for phased array applications.

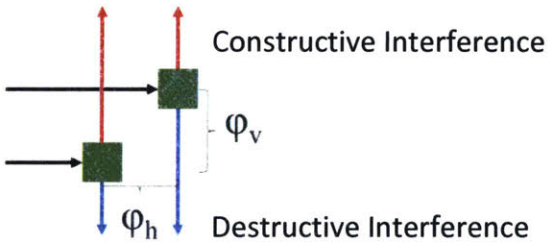

Figure 3.6. Conceptual schematic of unidirectional emission enabled by offset scattering points in a grating structure.

A unidirectional silicon nitride antenna for 635 nm emission was designed in this work. The 300 mm wafer fabrication process used in this work includes two 200 nm thick silicon nitride layers that may be independently patterned. Emission unidirectionality was imposed by patterning offset perturbations in a dual-layer silicon nitride waveguide structure, as shown in Fig. 3.7. Perturbations are

implemented in a similar manner to that shown in the previous section, by decreasing the width of the waveguide as compared to an initial width. The different waveguide regions that constitute a single period in a unidirectional antenna, along with example mode profiles, are illustrated in Fig. 3.7. The offset of the perturbation between the two silicon nitride layers along the direction of propagation determine the effective horizontal phase difference between scattering points in a grating period. The vertical phase difference is determined by the separation between the two silicon nitride layers, which is 100 nm is this case.

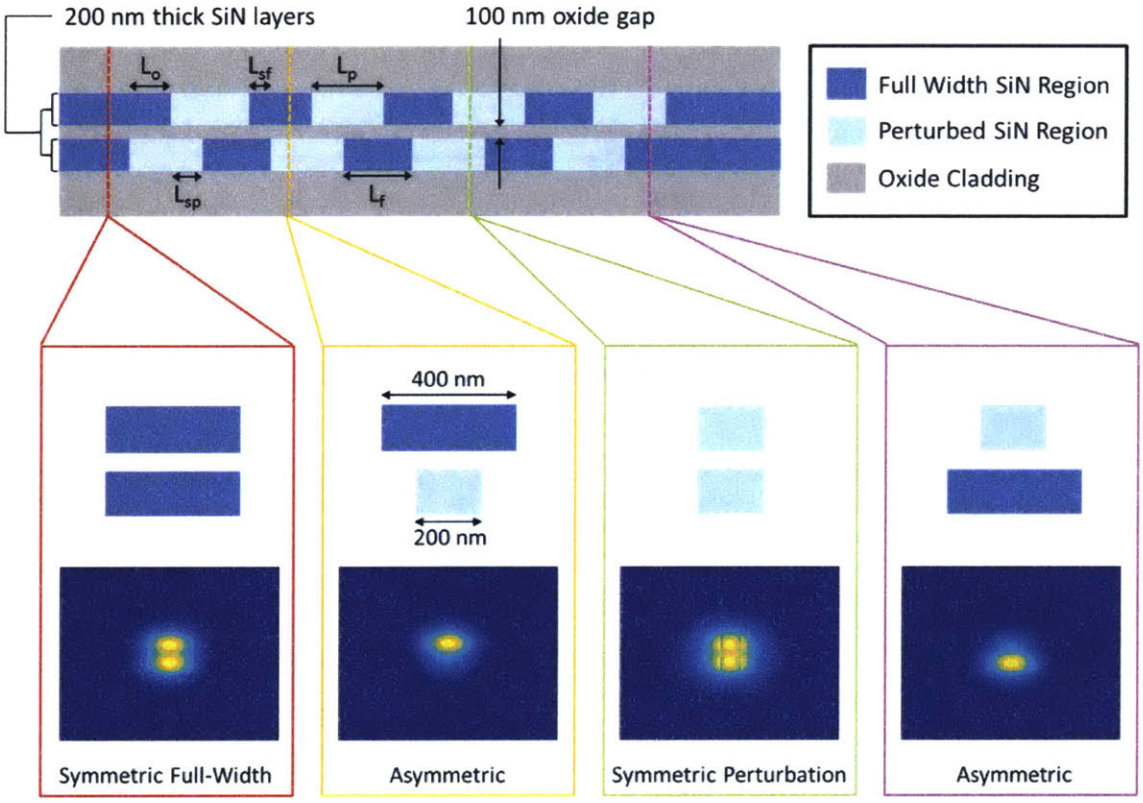

Figure 3.7. Schematic of the red dual-layer unidirectional antenna design with mode profiles shown for the four grating period sections for a select design parameter set.

As in the case of the symmetric emission antennas discussed in the previous section, the phase retardation of every grating period must be kept constant while varying the offset or perturbation along the length of the antenna. To design an

antenna that emits directly upwards, the following equality must be imposed on the lengths of the different regions within a grating period

$$L_{sf}n_f + L_{sp}n_p + 2L_a n_a = \lambda \tag{3.2}$$

where L_{sf}, L_{sp}, and L_a are the lengths of the lengths of the symmetric full-width, symmetric perturbation, and asymmetric regions, as labeled in Fig. 3.7. The quantities n_f, n_p, and n_a are the effective indices of the symmetric full-width, symmetric perturbation, and asymmetric regions. The lengths L_f and L_p of the full-width and perturbed waveguide regions, respectively, in a single layer as shown in Fig. 3.7 are related to L_{sf}, L_{sp}, and L_a as

$$L_f = L_{sf} + L_a, \qquad L_p = L_{sp} + L_a \tag{3.3}$$

These quantities are useful when translating simulated design to device layout. It is difficult to know the exact vertical phase differences present in this structure. Therefore, the first step in the antenna synthesis process is a parameter sweep to determine the offset, or the length of the asymmetric region, yielding the highest unidirectionality for a certain perturbation, which specifically gives the necessary offset phase delay for maximum unidirectionality. When varying the perturbation, the effective indices n_p and n_a of the symmetric perturbation and asymmetric regions are first calculated using an eigenmode solver. For a given perturbation, the length L_{sf} of the symmetric full-width region and the phase delay $\frac{2\pi L_a n_a}{\lambda}$ in the asymmetric region are kept constant while the length L_{sp} is altered to maintain a 2π phase delay within a period.

Simulated far fields of the downward and upward emissions of an optimized antenna design are shown in Fig. 3.8(a-b). A plot of directionality versus perturbation offset is also shown to demonstrate the parameter sweep. It should also be noted that a vertical phase difference of exactly $\lambda/4$ given is not possible the predetermined material layer stack, but only destructive interference in one direction is nominally needed for unidirectional emission. In this scenario, perfect constructive interference

is not observed in the emission direction, which decreases the effective perturbation strength of the grating. A plot of the emission versus perturbation as defined previously is shown in Fig. 3.8(d).

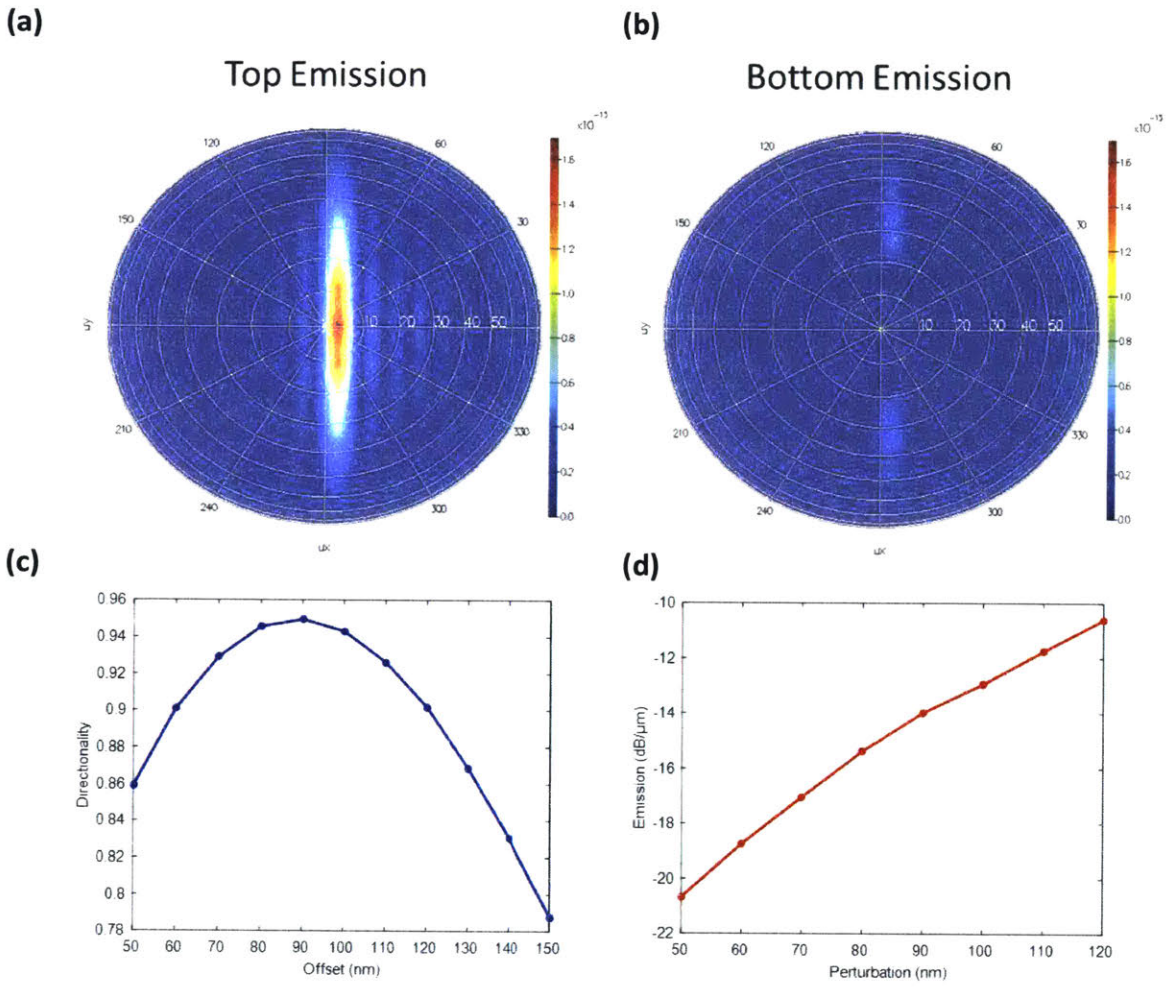

Figure 3.8. Simulated far field of the (a) top and (b) bottom emissions of an optimized unidirectional waveguide grating antenna. (c) Emission directionality versus offset length. (d) Emission versus perturbation strength.

A similar unidirectional antenna structure using two layers of silicon nitride was designed for 1550 nm operation. While 1550 nm waveguide grating antennas for phased arrays have primarily been implemented in silicon, silicon nitride provides the advantage that low optical confinement affords greater control over the perturbation strength and requires larger waveguide widths that render the device

more tolerant to fabrication errors. For example, a 100 nm perturbation in a single mode silicon nitride waveguide is approximately equivalent to a perturbation that is an order of magnitude smaller in a single mode silicon waveguide. Additionally, the rate at which the perturbation strength changes with a change in waveguide perturbation is much lower in silicon nitride than in silicon, which means that deviations from target waveguide widths during the lithographic patterning process will not significantly alter the perturbation strength. The simulated far-fields of the upwards and downward emission of an antenna for a waveguide grating antenna with a 1.2 μm full width and 0.135 μm perturbation are shown in Fig. 3.9(a-b). Plots

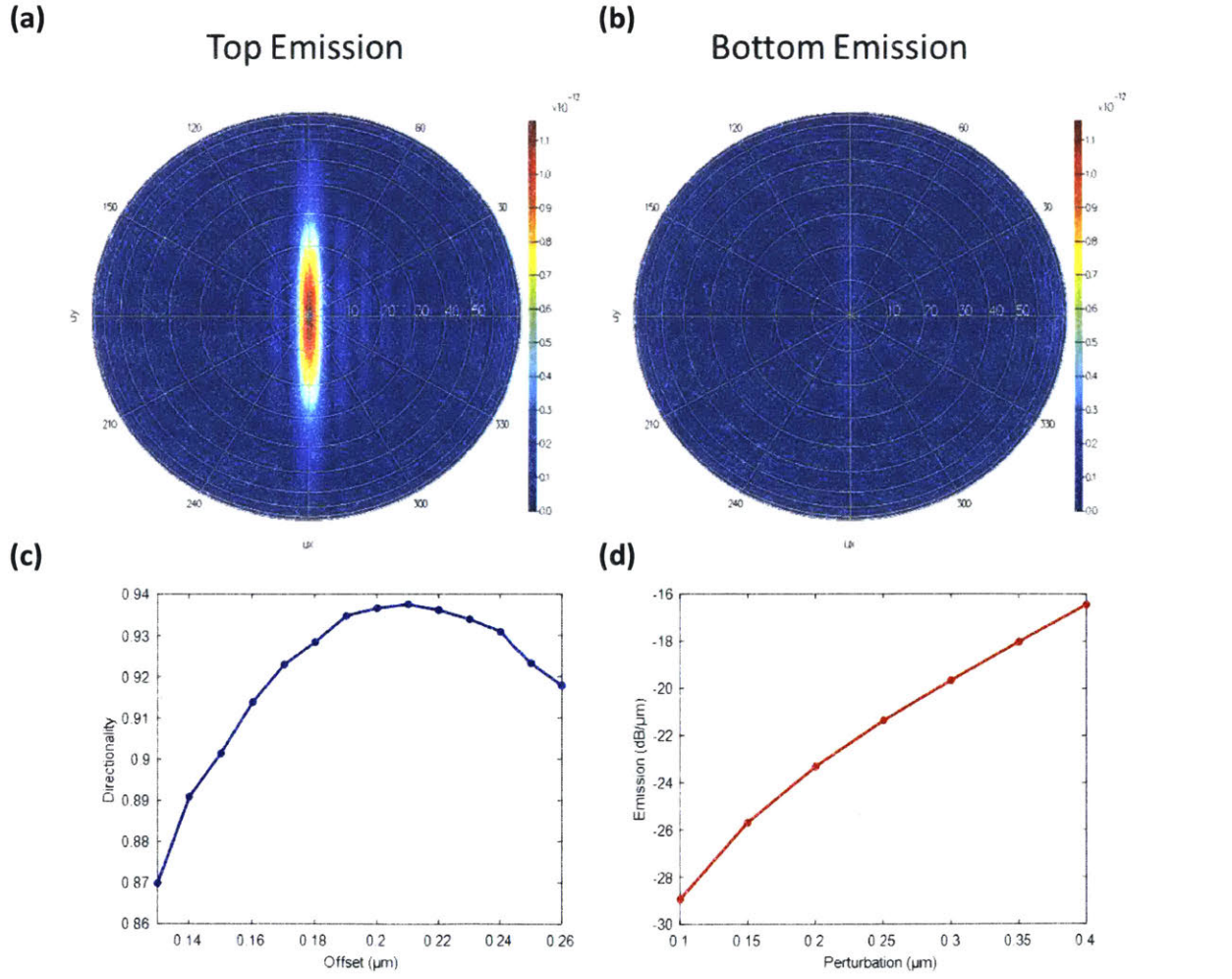

Figure 3.9. Simulated far field of the (a) top and (b) bottom emissions of an optimized unidirectional waveguide grating antenna. (c) Emission directionality versus offset length. (d) Emission versus perturbation strength.

of directionality versus offset and emission versus perturbation value are shown in Fig. 3.9(c-d)

While the upward emission of the waveguide grating antenna exits the chip without much reflection, the downward emission experiences significant reflections from the SiO_2-Si interface and the Si-air interface at the bottom of the substrate [48].

Fig. 3.10(a) shows a diagram depicting these reflections. Multiple reflections between these two interfaces results in the formation of concentric interference fringes in the far field of the phased array. A derivation of the geometric series describing the far-field intensity at a given angle θ assuming optical antennas emit as point sources is given in [48]. These interference fringes were observed in the far fields of the 64×64 unit cell passive optical phased array discussed earlier and are shown in Fig. 3.10(b-c). The visibility of these fringes may be used as a measure of the unidirectionality of an antenna. The measured far-fields of a symmetric mono-layer silicon nitride waveguide grating antenna and a dual-layer unidirectional antenna with the design discussed above, both designed for 1550 nm operation, are shown in Fig. 3.10(c-d). The visibility of fringes resulting from multiple reflections in the silicon substrate is significantly lower in the dual-layer antenna, thereby demonstrating high unidirectionality. This phenomenon is not observed in the case of visible light antennas, since visible is absorbed in the silicon substrate.

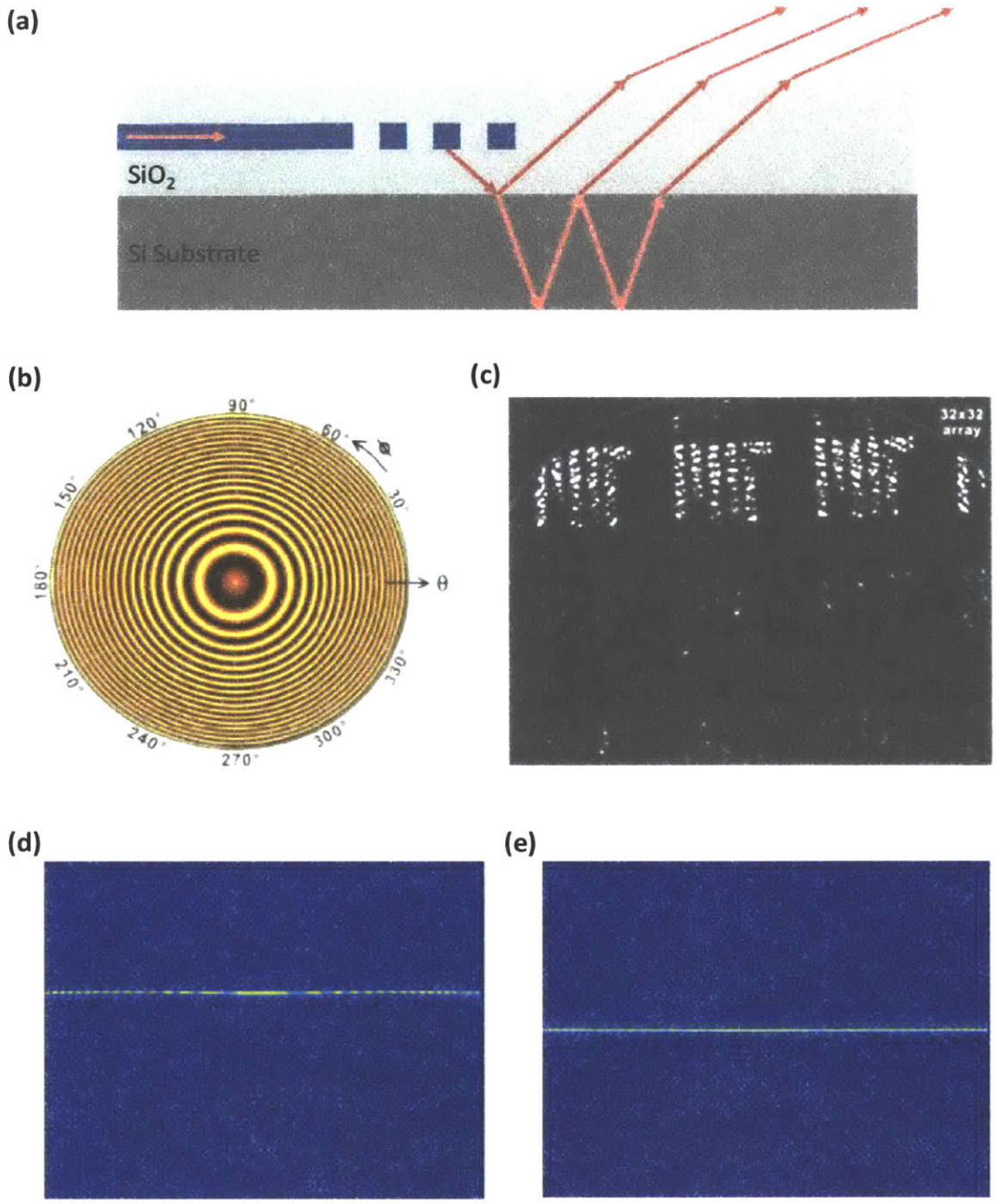

Figure 3.10. (a) Reflections from bottom emissions of grating, resulting in concentric rings in the far-field as shown in (b). (c) Measured far field of the 64×64 unit cell passive optical phased array with visible concentric rings. (d) Measured far field of a single monolayer 1550 nm waveguide grating antenna with visible concentric rings. (e) Measured far field of a single unidirectional 1550 nm waveguide grating antenna exhibiting significantly suppressed concentric fringes.

4 Integrated Liquid Crystal Phase Modulation

While previous chapters presented the ability to implement large-scale visible light phased array systems and the promise of visible light integrated optical phased arrays systems for 3D image projection, all demonstrated devices were passive. Practical applications of visible light phased arrays, such as 3D video [9], holographic bio-imaging [49], and neuronal targeting for optogenetics [11] would require that the phased array be dynamically reconfigurable. Active tuning of antenna phases must be implemented for this purpose. Unfortunately, silicon nitride does not have an appreciable thermo-optic coefficient nor does it exhibit any significant electro-optic effects, thereby posing a significant challenge for implementing integrated phase tuning. Phase modulation must therefore be carried out using a mechanism external to the silicon nitride material. Nematic liquid crystals (LCs) exhibit strong birefringence in the visible spectrum, which makes them ideally suited for this purpose. An integrated waveguide with a nematic liquid crystal cladding layer was therefore chosen as the phase modulation device. The following sections discuss the theory of operation of liquid crystals for phase-only modulation as well as the design and characterization of a liquid-crystal-based integrated phase modulator.

4.1 Theory of Liquid Crystal Phase Modulation

Nematic liquid crystal molecules exhibit high optical birefringence between the ordinary and extraordinary axes, as shown in Fig. 4.1(a), and will reorient to the electric field lines generated by a voltage applied across the liquid crystal layer [50].

In order to implement phase-only modulation, a voltage is applied across a nematic liquid crystal layer to induce a phase delay proportional to the orientation of liquid crystal molecules with respect to the direction of propagation of light. Operation of liquid crystals in this manner is referred to as electrically controlled birefringence (ECB).

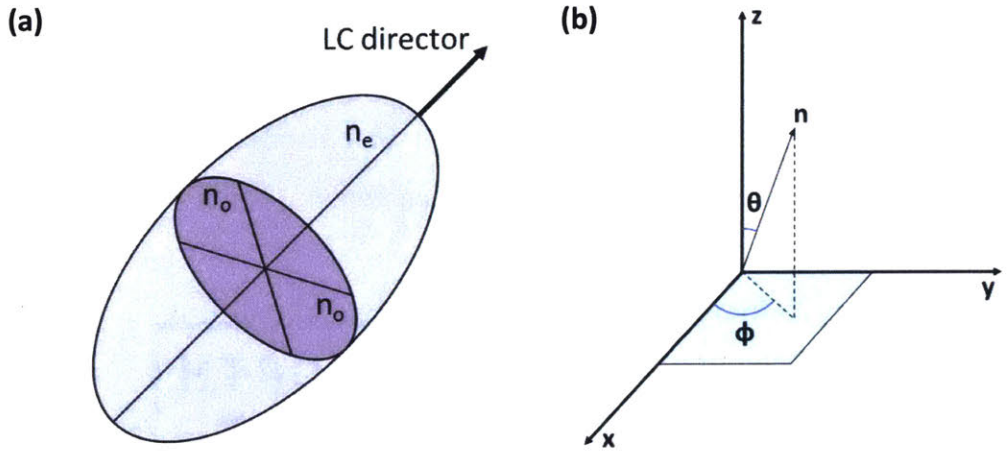

Figure 4.1. (a) Diagram of a liquid crystal (LC) molecule with ordinary and extraordinary axes labeled with respect to the director $\boldsymbol{n}$. (b) The coordinate system which will be used in this section for defining the alignment of the director.

Precise modeling of nematic liquid crystal molecules is very difficult due to the transition in molecular orientation from a surface to bulk liquid crystal, especially in the presence of an electric or magnetic field [51]. An understanding of nematic liquid crystal dynamics may yet be achieved via an analysis with respect to the free energy of the system. In a liquid crystal cell comprised of two flat surfaces with bulk material in between, surface interactions anchor liquid crystals to a certain alignment. The scenario in which all molecules in the liquid crystal cell have the same alignment as that determined by the surface anchoring is an equilibrium state with the lowest possible free energy [52]. Deviations from this equilibrium will lead to an increase in the free energy of the system. The free energy density of a bulk liquid crystal system can be expressed as

$$f = f_0 + f_d \tag{4.1}$$

where f_0 is the undistorted free energy density and f_d is the Frank-Oseen elastic free energy density which arises due to bulk distortions of liquid crystal molecules away from their equilibrium positions. The Frank-Oseen free energy density is given by

$$f_d = \frac{1}{2}k_1(\nabla \cdot \hat{\mathbf{n}})^2 + k_2(\hat{\mathbf{n}} \cdot \nabla \times \hat{\mathbf{n}})^2 + k_3(\hat{\mathbf{n}} \times \nabla \times \hat{\mathbf{n}})^2 \tag{4.2}$$

where k_1, k_2, *and* k_3 are the Frank elastic constants for splay, twist, and bend, respectively [53]. An illustration of these three constants is shown in Fig. 4.2. Each of the three terms in Equation 4.2 quantifies the energy penalty for its associated distortion.

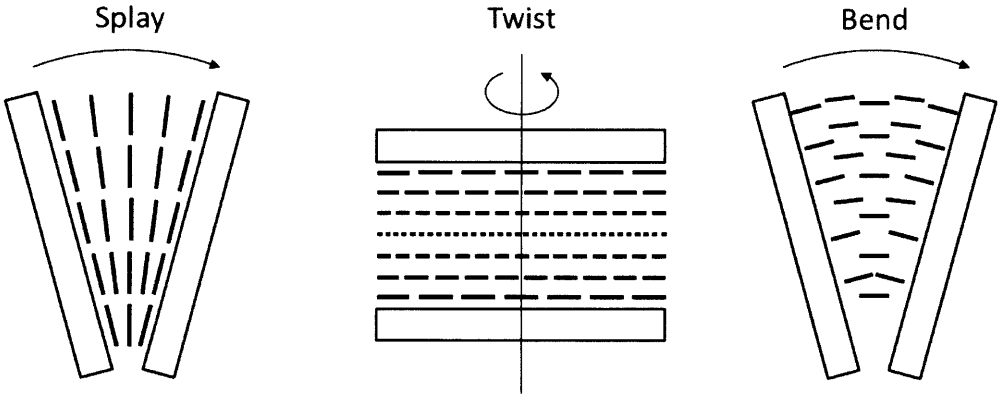

Figure 4.2. Distortions in nematic liquid crystals: (a) splay, (b) twist, and (c) bend.

It is often the case that the three Frank elastic constants are of the same order and approximately the same amplitude. Therefore, for the purpose of simplifying the mathematical modeling of nematic liquid crystal systems, the one-elastic constant approximation, in which $k_1 = k_2 = k_3 = k$, may be used to rewrite Equation 4.2 as

$$f_d = \frac{1}{2}k[(\nabla \cdot \hat{\mathbf{n}})^2 + (\nabla \times \hat{\mathbf{n}})^2] \tag{4.3}$$

The total free energy of a bulk liquid crystal sample is then given by the volume integral

$$F = \int_v f d^3r f_d = \frac{1}{2}k[(\nabla \cdot \hat{\mathbf{n}})^2 + (\nabla \times \hat{\mathbf{n}})^2] \tag{4.4}$$

where v is the volume of the sample of liquid crystal cell. The equilibrium alignment of liquid crystal directors in the cell is then found by minimizing the total free energy F by solving the Euler-Lagrange equations for the bulk free energy density given as

$$\frac{\partial f}{\partial \theta} - \frac{d}{dz}\left[\frac{\partial f}{\partial \theta'}\right] = 0, \qquad \frac{\partial f}{\partial \phi} - \frac{d}{dz}\left[\frac{\partial f}{\partial \phi'}\right] = 0 \tag{4.5}$$

where θ and ϕ are as defined in Fig. 4.1(b), and $\theta' = \frac{\partial \theta}{\partial z}$ and $\phi' = \frac{\partial \phi}{\partial z}$ [54-55]. The above equations have the following boundary conditions

$$\pm\frac{\partial f}{\partial \theta'} = 0, \qquad \pm\frac{\partial f}{\partial \phi'} = 0 \tag{4.6}$$

In a liquid crystal cell, molecular interactions at the surfaces differ greatly from those in the bulk due to anchoring forces experienced by the molecules at these interfaces. The free surface energy of liquid crystals must therefore be modeled in a different manner than the bulk free energy discussed above. Two anchoring conditions, weak and strong, are of relevance to this work. Anchoring conditions may be seen as a modification to the boundary conditions of Equation 4.6. In the case of strong anchoring, there are no modifications to the above boundary conditions except that certain conditions, such as the director angle at the surface, must be imposed depending on the specific scenario [53]. Two common alignment configurations with strong anchoring, namely *homeotropic*, in which molecules are aligned perpendicular to the surface, and *homogeneous*, in which molecules are aligned parallel to the surface, are shown in Fig. 4.3.

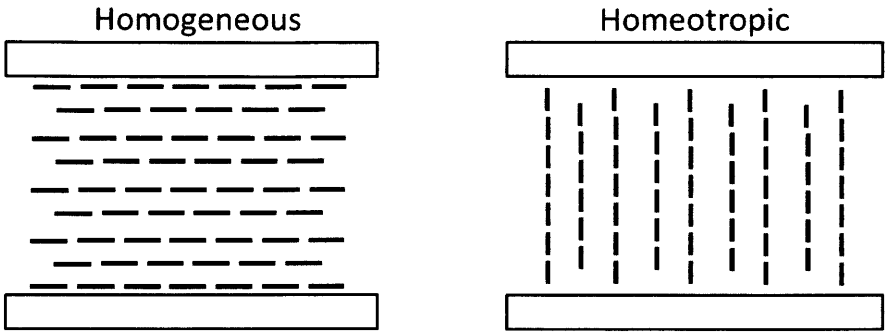

Figure 4.3. Homogeneous and homeotropic alignment of liquid crystals in a cell.

In the case of weak anchoring, where the director angle at the surface may change in the presence of applied fields, a separate expression for the surface free energy must be introduced. The Rapini-Papoular approximation, often used to express the surface energy, is shown below

$$F_s = \frac{W}{2}\sin^2\alpha \tag{4.7}$$

where W is the anchoring strength and α is an angle representing the director deviation [53]. This approximation results in a modification of the boundary condition in Equation 4.6 as follows

$$-\left[\frac{\partial f}{\partial \theta'}\right]_1 + \frac{\partial f_1}{\partial \theta_1'} = 0, \qquad -\left[\frac{\partial f}{\partial \phi'}\right]_1 + \frac{\partial f_1}{\partial \phi_1'} = 0 \tag{4.8}$$

$$\left[\frac{\partial f}{\partial \theta'}\right]_2 + \frac{\partial f_2}{\partial \theta_2'} = 0, \qquad \left[\frac{\partial f}{\partial \phi'}\right]_2 + \frac{\partial f_2}{\partial \phi_2'} = 0 \tag{4.9}$$

where the subscripted indices refer to the top (*1*) and bottom (*2*) surfaces in a liquid crystal cell.

Liquid crystal molecules in the bulk of a cell will reorient themselves upon application of an external electric or magnetic field. This reorientation is known as the Frederick Transition. The examples presented in the remainder of this section to

describe the Frederick Transition will be one-dimensional, with only θ changing along the thickness of the cell. This situation sufficiently represents the liquid crystal system, shown in Fig. 4.4, with which the remainder of this work will be concerned. We first consider the formulation of the energy density contribution of an externally applied electric field. The application of an electric field across a liquid crystal cell gives rise to a dipole moment per unit volume **P**, also called the polarization [53]. For simplicity, **n** is assumed to be in the direction of the z-axis. **P** is related to **E** by the electric susceptibility tensor as shown below

$$\mathbf{P} = \varepsilon_0 \boldsymbol{\chi}_\mathbf{e} \mathbf{E} \tag{4.10}$$

$$\boldsymbol{\chi}_\mathbf{e} = \begin{bmatrix} \chi_{e_\perp} & 0 & 0 \\ 0 & \chi_{e_\perp} & 0 \\ 0 & 0 & \chi_{e_\parallel} \end{bmatrix} \tag{4.11}$$

where $\chi_{e_\perp}$ and $\chi_{e_\parallel}$ are the electric susceptibilities perpendicular and parallel to the director, respectively. The electric displacement **D** may then be written as follows

$$\mathbf{D} = \varepsilon_0 \mathbf{E} + \mathbf{P} = \varepsilon_0 \boldsymbol{\epsilon} \mathbf{E} \tag{4.12}$$

$$\boldsymbol{\varepsilon} = \mathbf{I} + \boldsymbol{\chi}_\mathbf{e} = \begin{bmatrix} \varepsilon_\perp & 0 & 0 \\ 0 & \varepsilon_\perp & 0 \\ 0 & 0 & \varepsilon_\parallel \end{bmatrix} \tag{4.13}$$

where $\varepsilon_\perp$ and $\varepsilon_\parallel$ are the relative dielectric permittivities when the director and field are perpendicular and parallel, respectively. The electric displacement may finally be defined as

$$\mathbf{D} = \varepsilon_0 \varepsilon_\perp + \varepsilon_0 \Delta\varepsilon (\mathbf{n} \cdot \mathbf{E}) \mathbf{n} \tag{4.14}$$

$$\Delta\varepsilon = \varepsilon_\parallel - \varepsilon_\perp \tag{4.15}$$

where $\Delta\varepsilon$ is referred to as the dielectric anisotropy of the liquid crystal. The electric energy density given a constant voltage applied across the cell is then given by

$$f_e = -\int_0^{\mathbf{E}} \mathbf{D} \cdot d\mathbf{E} = -\frac{1}{2}\mathbf{D} \cdot \mathbf{E} = -\frac{1}{2}\varepsilon_0\varepsilon_\perp E^2 - \frac{1}{2}\varepsilon_0\Delta\varepsilon(\mathbf{n} \cdot \mathbf{E})^2 \tag{4.16}$$

The first term of the last expression in 4.16 is generally omitted in calculations of free energy since it is independent of molecular orientation, thereby yielding the following expression

$$f_e = -\frac{1}{2}\varepsilon_0\Delta\varepsilon(\mathbf{n} \cdot \mathbf{E})^2 \tag{4.17}$$

The total free energy of a liquid crystal cell assuming the one-elastic-constant approximation is expressed below

$$F = \frac{1}{2}\int_0^d dz\left[k_i\left(\frac{d\theta(z)}{dz}\right)^2 - |\Delta\varepsilon|E^2\sin^2\theta(z)\right] + \frac{W_1}{2}\sin^2\theta_1 + \frac{W_2}{2}\sin^2\theta_2 \tag{4.18}$$

where k_i is the one-elastic constant, and the subscripted indices *1* and *2* denote values at the top and bottom surfaces, respectively. A variational approach is generally taken to find the minimum value of the functional in Equation 4.18, but some assumptions and simplifications will be made in the following discussion in order to gain some intuition for certain aspects of liquid crystal behavior. Equation 4.19 and the following derivations are as seen in [54-55]. With the small angle approximation applied to θ, the following equilibrium equation is obtained in the presence of a constant electric field

$$\frac{d^2\theta(z)}{dz^2} + \xi^2\theta = 0 \tag{4.19}$$

where $\xi = E\sqrt{|\Delta\varepsilon|/k_i}$. Equation 4.19 has boundary conditions

$$-k_i \frac{d\theta(z)}{dz} + W_1\theta_1 = 0, \qquad z = 0 \tag{4.20}$$

$$k_i \frac{d\theta(z)}{dz} + W_2\theta_2 = 0, \qquad z = d \tag{4.21}$$

The solution of this equilibrium equation shown above has the form

$$\theta(z) = a\sin(\xi z) + b\cos(\xi z) \tag{4.22}$$

This solution yields the following two relations for a and b.

$$\theta(0) = b, \qquad \frac{d\theta(0)}{dz} = \xi a \tag{4.23}$$

which in turn yields the following relationship upon substitution in 4.20.

$$\frac{a}{b} = \frac{W}{\xi k_i} \tag{4.24}$$

Furthermore, assuming the two surfaces are identical results in a deformation that is symmetric with a maximum at $z = d/2$, which results in a more specific definition of Equation 4.24 as

$$\frac{a}{b} = \tan\left(\frac{\xi d}{2}\right) \tag{4.25}$$

This in turn yields an expression for the anchoring strength as

$$W = \xi k_i \tan\left(\frac{\xi d}{2}\right) \tag{4.26}$$

In the case of strong anchoring ($W \to \infty$), the surface direction orientation is maintained, thereby imposing the following conditions

$$\theta(0) = \theta(d) = 0 \longrightarrow b = a\sin(\xi d) = 0 \tag{4.27}$$

It can be seen from Equation 4.26 that for the strong anchoring case, $\xi = \pi/d$, which yields an expression for the threshold electric field, which is the minimum field strength needed to cause a distortion in the bulk

$$E_{th} = \frac{\pi}{d}\sqrt{\frac{k_i}{|\Delta\varepsilon|}} \tag{4.28}$$

An illustration of this threshold mechanism is shown in Fig. 4.4.

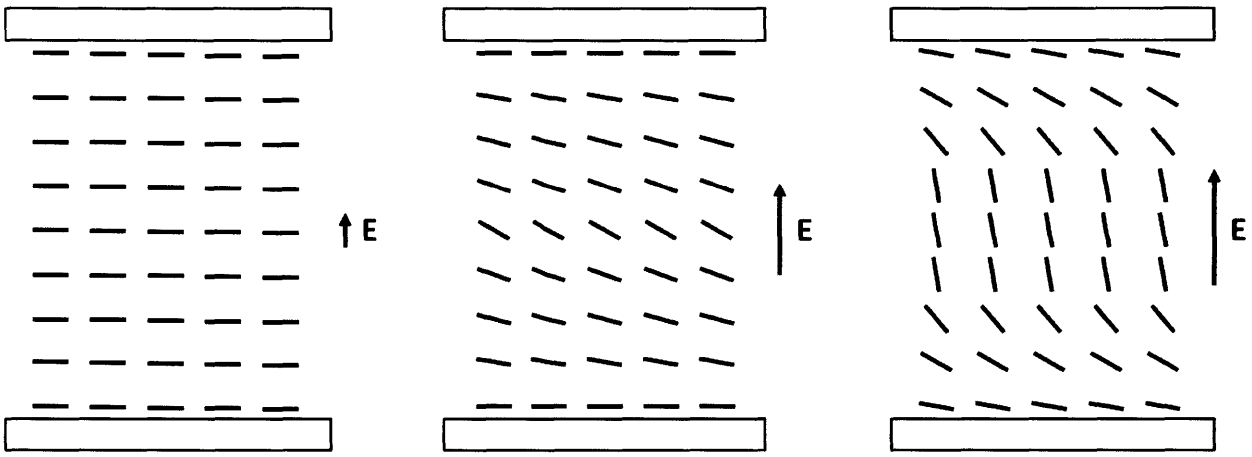

Figure 4.4. Illustration of the threshold mechanism in liquid crystal cells. Molecules do not reorient until the amplitude of the applied field is above a certain threshold value and molecules anchored to surface do not experience significant rotation.

4.2 ECB Characterization

To demonstrate the phase tuning capabilities of liquid crystals, a liquid crystal cell for electrically controlled birefringence was manufactured and characterized. Liquid crystal mixture 5CB was used for this experiment. The cell was comprised of two indium tin oxide (ITO) coated slides glued together with an SU-8 spacer layer in between. Both ITO slides were also coated with a very thin film of polyimide and rubbed in an antiparallel configuration to anchor cells at the surface with a small pretilt angle. The fabrication process for the liquid crystal cell is outlined in Fig. 4.5.

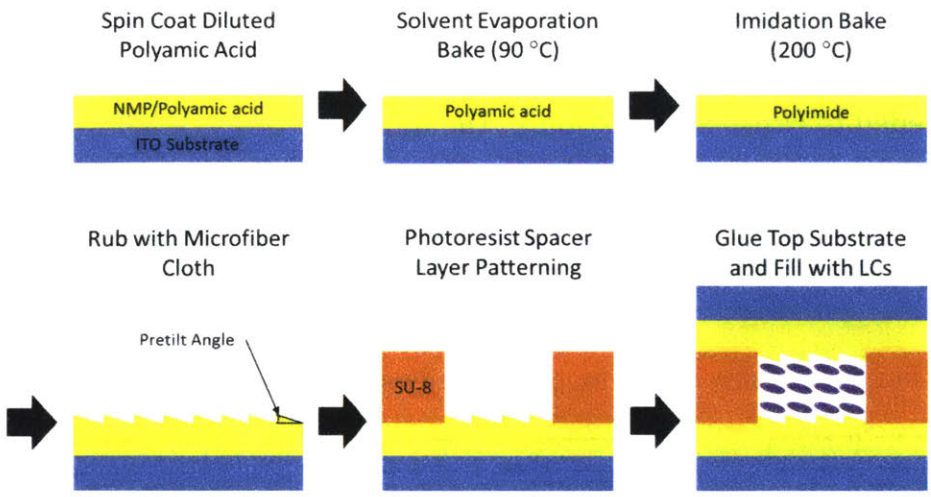

Figure 4.5. Fabrication process flow for constructing a liquid crystal cell with anti-parallel polyimide alignment.

A tabletop Michelson interferometer, as shown in Fig. 4.6, was used to characterize the fabricated liquid crystal cell. Specifically, the cell was placed in one of the arms of the interferometer and the relative phased difference between the two arms upon applying a voltage across the two ITO electrodes was measured from the interference fringes formed at the output. The voltage applied to the cell is an AC signal. If a constant voltage is applied to the cell, charge accumulation at one of the electrode interfaces will cause permanent damage to the alignment layer [56]. The use of an AC signal with an RMS voltage equal to the desired voltage amplitude, a technique referred to as polarity inversion, is generally used to neutralize this effect [56]. The polarity inversion scheme used in this work utilizes a 2kHz AC carrier signal. The liquid crystal responds to the RMS voltage of this signal [57].

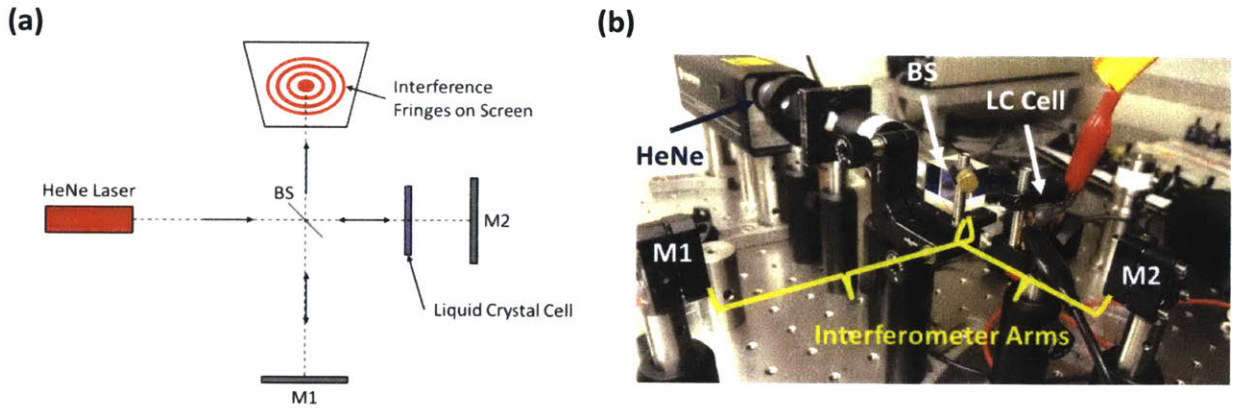

Figure 4.6. (a) Schematic of the tabletop Michelson interferometer comprised of a HeNe laser, a beamsplitter (BS), and two mirrors M1 and M2. (b) An image of the tabletop Michelson interferometer.

Fig. 4.7(a) shows the phase shift versus voltage of a commercial liquid crystal cell with a known cell thickness, which was used as a control. The extrapolated maximum attainable index shift of the liquid crystal in the presented cell geometry was 0.127. A graph of the phase shift of the fabricated cell is shown in Fig. 4.7(b). The cell was fabricated with a target thickness of 10 μm, but errors in the fabrication may cause significant deviations from this value. For instance, a thickness of 10 μm was targeted based on a thickness versus spin rate curve of SU-8. Errors in the spin rate may cause errors in cell thickness. A commercial liquid crystal cell with a known cell thickness was therefore used as a control. An approximation of the cell thickness L may then be obtained from using the following relation

$$L = \frac{\varphi\lambda}{2\pi\Delta n} \tag{4.29}$$

where Δn is maximum attainable index shift, φ is the measured phase shift, and λ is the wavelength of the incident light. The final thickness of the fabricated cell based on the maximum index shift was 16.25 μm. The phase response of the cell is relatively linear within a certain voltage range, as shown in Fig. 4.7. A $V_\pi L$ of 2.113×10^{-4} V·cm was obtained for operation within this linear regime.

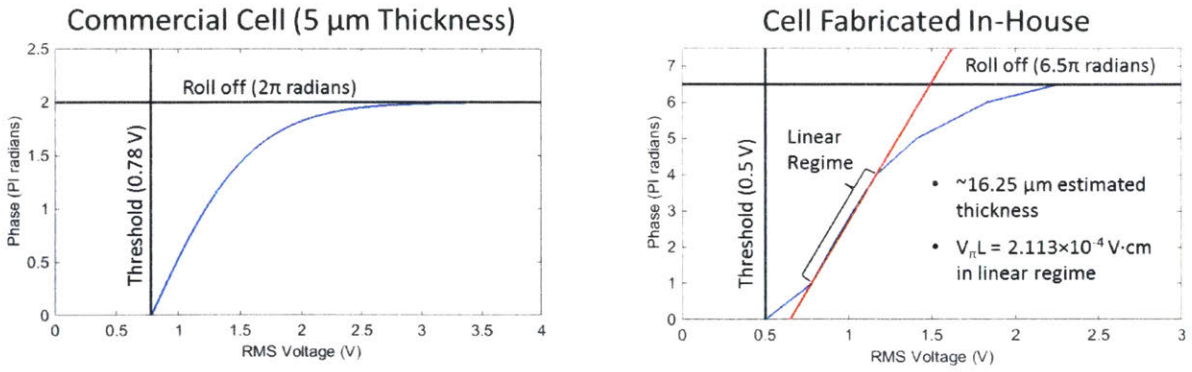

Figure 4.7. Measured phase versus voltage of control (5 μm thickness) and fabricated liquid crystal cells.

4.3 Integrated Phase Modulation

The eventual goal is to implement integrated visible light phase modulators based on liquid crystals for incorporation into large scale photonic integrated circuits. Integrated waveguides with tunable index cladding materials have been commonplace in the photonics research sphere for the purposes of both modulation and sensing [51,57,58]. In such a device, the evanescent field of a mode supported by the integrated waveguide interacts directly with the tunable cladding. A change in refractive index leads to a change in the effective refractive index of the mode. For the purpose of phased modulation in the visible spectrum, a silicon nitride waveguide with a liquid crystal cladding may be used. Specifically, the evanescent field of a quasi-TE mode propagating in the waveguide will see a shift in the cladding index if the orientation of the liquid crystal director is tuned to an angle with respect to the propagating electric field in a plane normal to the direction of propagation, as shown in Fig. 4.8. Liquid crystal is an ideally suited material for this purpose since it is transparent in the visible spectrum and may be engineered to have very high optical anisotropy.

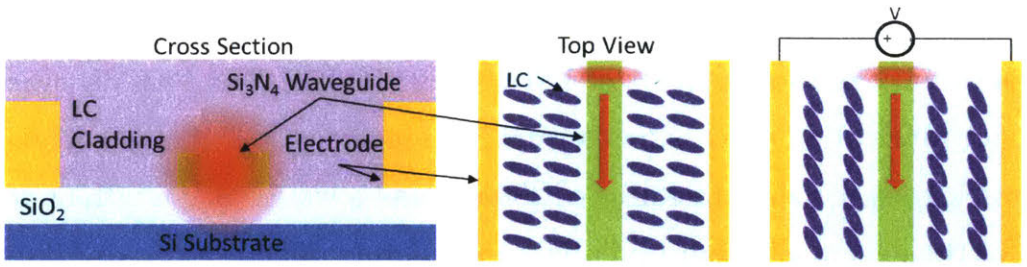

Figure 4.8. Cross-section of integrated liquid crystal phase modulator and schematic of phase tuning upon voltage application.

The fabrication process for the integrated liquid crystal phase modulator is shown in Fig. 4.9. The process specifically outlines the integration of a liquid crystal layer atop the silicon nitride layer that has already been patterned in the previously mentioned 300 mm wafer process.

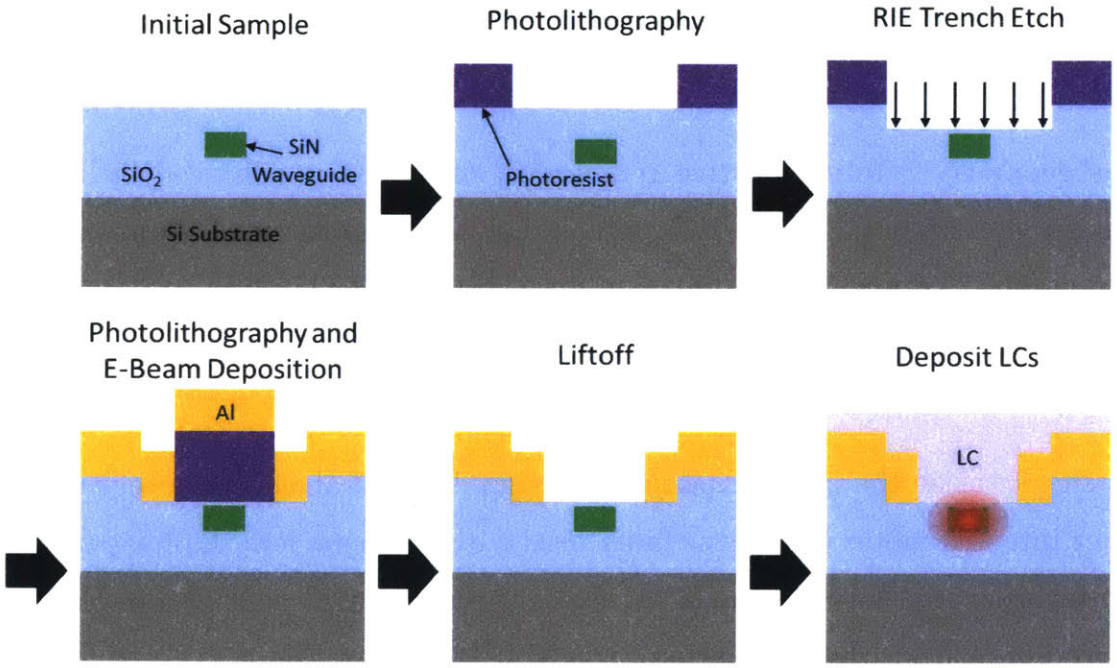

Figure 4.9. Fabrication process flow for the incorporation of an overlying liquid crystal cladding layer for implementing the integrated visible light phase modulator.

At a wavelength of 635 nm, 5CB has an ordinary refractive index of 1.5317 and an extraordinary refractive index of 1.7056 at 25 °C [59]. The PECVD silicon nitride used in our fabrication process has a refractive index of 1.98 at this wavelength. The silicon nitride layer has a thickness of 200 nm and a waveguide width of 360 nm was chosen for the design of integrated phase modulators. Mode solver simulations of the liquid crystal clad silicon nitride waveguide through a range of possible 5CB refractive indices is shown in Fig. 4.10.

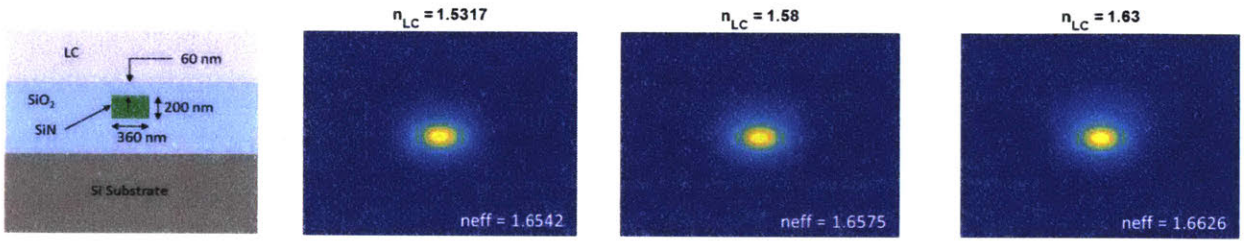

Figure 4.10. Cross section of waveguide with overlying liquid crystal layer and mode profiles for three different liquid crystal cladding indices.

In this geometry a total effective index shift of 0.0084 is achieved by tuning the cladding index from 1.5317 to 1.63, which enables 2π phase modulation in a device length of only 75.6 μm. Tuning the liquid crystal to higher indices is not carried out in this design since doing so reduces the confinement of the mode in silicon nitride and results in significant insertion loss.

To characterize the phase modulator design detailed above, an integrated Mach-Zehnder interferometer (MZI) was fabricated with a 100 μm length phase modulation region incorporated into each arm. A schematic of the MZI is shown in Fig. 4.11(a). Measured data from the two ports of the MZI, shown in Fig. 4.11(b), show a phase shift of approximately π.

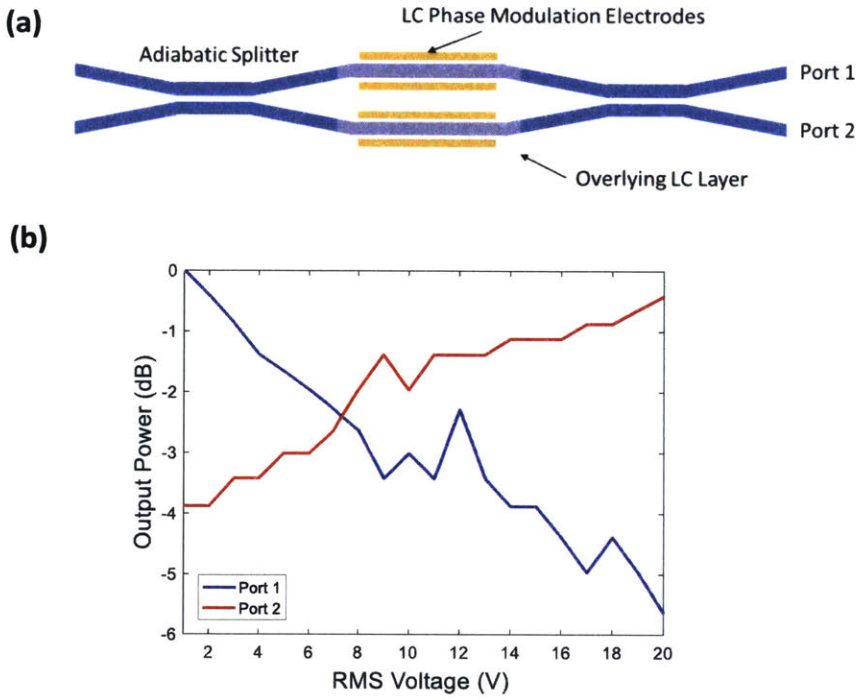

Figure 4.11. (a) Schematic of an integrated MZI with liquid crystal based phase modulators in each arm. (b) Measured output response of the fabricated MZI device.

Unfortunately, errors in the thickness of the overlying oxide cladding layer upon carrying out PECVD deposition and RIE etching of the top oxide cladding prevented a more accurate measurement of the phase tuning capability of the integrated phase modulator. Despite this setback, the measured data demonstrates the promise of integrated liquid crystal phase modulation and an optimization of the fabrication process in order to achieve 2π phase modulation is currently underway.

5 Conclusion

The work presented in this thesis is the first in-depth investigation of integrated optical phased arrays in the visible spectrum. The 32×32 emitter passive phased arrays shown in Section 2.3 are the first integrated visible phased arrays presented to date. Furthermore, the work presented in Chapter 2 demonstrated the promise that phased array technology holds for the realization of glass-free 3D microdisplays in the future. Because of their ability to generate highly directional radiation patterns, phased arrays are well suited for accurately reproducing the light fields of virtual objects for autostereoscopic display applications. This capability was demonstrated with a system of 16 integrated optical phased arrays encoded to project a perspective image of a pyramid with parallax in one dimension, as shown in Section 2.3.

Further advancements in phased array autostereoscopy will require three primary developments. The first is the realization of compact integrated phase modulators to enable dynamically reconfigurable phased array systems for 3D video applications. Liquid-crystal-based modulation techniques may be used, but a robust and low-loss visible light modulator design must be developed. The work presented in Chapter 4 is the first step in this direction. Once an easily reproducible modulator design is realized, it may be incorporated into phased arrays to demonstrate beam steering and eventually more complex tasks such as arbitrary far-field pattern generation.

The second necessary development is the implementation of larger scale visible light phased arrays. Larger aperture phased arrays are capable of generating smaller diffraction limited spots, which would increase image resolution if used in autostereoscopic display applications. Additionally, the ability to fabricate large systems of phased arrays on a single chip would enable the expansion of the image projection system detailed in Chapter 2 to one that exhibits parallax in both

dimensions without the need for an asymmetric diffuser or any other external optics. The highly uniform 300 mm wafer CMOS process used to fabricate all the devices presented in this thesis will be an enabling factor in efforts to develop larger scale visible light phased arrays.

Lastly, phase modulators and phased arrays must be successfully demonstrated for lower wavelengths in the visible spectrum. As discussed in Section 3.3, it will be necessary to design high efficiency interfaces for coupling off-chip light into a photonic integrated circuit and optimizing material deposition recipes to produce low loss waveguide layers for these wavelengths.

Highly directional visible light also has uses in biomedical applications such as biofluorescence imaging and optogenetics. Robust visible light phased array platforms will enable the exploration of low-cost chip-scale optical devices for these applications. In the future, we fully intend to pursue the development of integrated phase modulators and large scale phased arrays in the visible spectrum with the goal of demonstrating large-scale reconfigurable autostereoscopic displays based on phased arrays as well as investigating novel application spaces for this technology.

6 Bibliography

[1] K. F. Braun, "Electrical oscillations and wireless telegraphy," *Nobel Lecture*, 1909.

[2] A. J. Fenn, D. H. Temme, W. P. Delaney, and W. E. Courtney, "The Development of Phased-Array Radar Technology," *Lincoln Laboratory Journal*, vol. 12, pp. 321-340, 2000.

[3] A. Yaacobi, J. Sun, M. Moresco, G. Leake, D. Coolbaugh, and M. R. Watts, "Integrated phased array for wide-angle beam steering," Opt. Lett., vol. 39, pp. 4575-4578, 2014.

[4] J. Sun, E. Timurdogan, A. Yaacobi, Z. Su, E. S. Hosseini, D. B. Cole, *et al.*, "Large-Scale Silicon Photonic Circuits for Optical Phased Arrays," *IEEE J. Sel. Top. Quant.*, vol. 20, pp. 264-278, 2014.

[5] J. Sun, E. Timurdogan, A. Yaacobi, E. Hosseini and M. R. Watts, "Large-Scale Nanophotonic Phased Array," *Nature*, vol. 493, no. 7431, 2013.

[6] J. C. Hulme, *et al.*, "Fully integrated hybrid silicon two dimensional beam scanner," *Opt. Express*, vol. 23, pp. 5861-5874, 2015.

[7] C. V. Poulton, A. Yaccobi, Z. Su, M. J. Byrd, and M. R. Watts, "Optical Phased Array with Small Spot Size, High Steering Range and Grouped Cascaded Phase Shifters," in *Advanced Photonics 2016 (IPR, NOMA, Sensors, Networks, SPPCom, SOF)*, OSA technical Digest (online) (Optical Society of America, 2016), paper IW1B.2, 2016.

[8] K. V. Acoleyen, W. Bogaerts, J. Jágerská, N. L. Thomas, R. Houdré, and R. Baets, "Off-chip beam steering with a one-dimensional optical phased array on silicon-on-insulator," *Opt. Lett.*, vol. 34, pp. 1477–1479, 2009.

[9] J. Hong *et al.*, "Three-dimensional display technologies of recent interest: principles, status, and issues [Invited]," *Appl. Opt.*, vol. 50, H87–H115, 2011.

[10] J. Geng, "Three-dimensional display technologies," *Adv. Opt. Photon.*, vol. 5, pp. 456-535, 2013.

[11] F. Zhang et al., "Optogenetic interrogation of neural circuits: technology for probing mammalian brain structures." *Nat. Protoc.*, vol. 5, pp. 439-456, 2010.

[12] R. L. Haupt, *Antenna arrays: a computational approach*, Wiley, New Jersey, 2010.

[13] H. A. Haus, *Waves and Fields in Optoelectronics*, Prentice Hall, New Jersey, 1984.

[14] J. Sun, A. Yaacobi, M. Moresco, D. D. Coolbaugh, and M. R. Watts, "Integrated Continuously Tunable Optical Orbital Angular Momentum Generator," *Conference on Lasers and Electro-Optics (CLEO),* Postdeadline Paper JTh5A.5, 2015.

[15] J. Sun, M. Moresco, G. Leake, D. Coolbaugh, and M. R. Watts, "Generating and identifying optical orbital angular momentum with silicon photonic circuits," *Opt. Lett.*, vol. 39, pp. 5977-5980, 2014.

[16] R. W. Gerchberg, and W. O. Saxton, "A practical algorithm for the determination of phase from image and diffraction plane pictures," *Optik*, vol. 35, pp. 237-246, 1972.

[17] A. Hosseini, D. Kwong, C. Lin, B. S. Lee, and R. T. Chen. "Output formulation for symmetrically excited one-to-multimode interference coupler," *IEEE J. Sel. Top. Quant.*, vol. 16 pp. 61–69, 2010.

[18] T. Okoshi, *Three-Dimensional Imaging Techniques*, Academic Press, New York, 1976.

[19] D. M. Hoffman, A. R. Girshick, K. Akeley, and M. S. Banks, "Vergence–accommodation conflicts hinder visual performance and cause visual fatigue," *J. Vis.*, vol. 8, 2008.

[20] W. P. Bleha and L. A. Lei, "Advances in Liquid Crystal on Silicon (LCOS) spatial light modulator technology," *Proc. SPIE 8736, Display Technologies and Applications for Defense, Security, and Avionics VII,* 87360A, 2013.

[21] D. Kim, "Reduction of coherent artifacts in dynamic holographic three-dimensional displays by diffraction-specific pseudorandom diffusion," *Opt. Lett.*, vol. 29, pp. 611-613, 2004.

[22] N. Bertaux, Y. Frauel, P. Réfrégier, and B. Javidi, "Speckle removal using a maximum-likelihood technique with isoline gray-level regularization," *J. Opt. Soc. Am. A*, vol. 21, pp. 2283-2291, 2004.

[23] J. Maycock *et al.*, "Reduction of speckle in digital holography by discrete Fourier filtering," *J. Opt. Soc. Am. A*, vol. 24, pp. 1617-1622, 2007.

[24] E. Adelson and J. Bergen, "The plenoptic function and the elements of early vision," in *Computational Models of Visual Processing*, MIT, pp. 3–20, 1991.

[25] M. Levoy, P. Hanrahan, "Light field rendering," *SIGGRAPH, 1996 Proceedings of the,* pp. 31-42, 1996.

[26] T. Peterka, R. L. Kooima, D. J. Sandin, A. Johnson, J. Leigh, and T. A. DeFanti, "Advances in the Dynallax solid-state dynamic parallax barrier autostereoscopic visualization display system," *IEEE Trans. Vis. Comput. Graph.*, vol. 14, pp. 487–499, 2008.

[27] G. Hamagishi, "Analysis and improvement of viewing conditions for two-view and multi-view 3D displays," in *SID International Symposium Digest of Technical Papers*, Society for Information Display, vol. 40, pp. 340–343, 2009.

[28] W. Hess, "Stereoscopic picture," U.S. patent 1,128,979, February 16, 1915.

[29] C. van Berkel and J. A. Clarke, "Characterization and optimization of 3D-LCD module design," *Proc. SPIE 3012, Stereoscopic Displays and Virtual Reality Systems IV*, pp. 179-186, 1997.

[30] Y. Takaki and N. Nago, "Multi-projection of lenticular displays to construct a 256-view super multi-view display," *Opt. Express*, vol. 18, pp. 8824–8835, 2010.

[31] J.-H. Park, Y. Kim, J. Kim, S.-W. Min, and B. Lee, "Three-dimensional display scheme based on integral imaging with three-dimensional information processing," *Opt. Express*, vol. 12, pp. 6020–6032, 2004.

[32] X. Xiao, B. Javidi, M. Martinez-Corral, and A. Stern, "Advances in three-dimensional integral imaging: sensing, display, and applications [Invited]," *Appl. Opt.*, vol. 52, pp. 546-560, 2013.

[33] G. Lippmann, "Epreuves reversibles donnant la sensation du relief," *J. Phys.*, vol. 7, pp. 821–825, 1908.

[34] Q. Zhong, Y. Peng, H. Li, C. Su, W. Shen, and X. Liu, "Multiview and light-field reconstruction algorithms for 360° multiple-projector-type 3D display," *Appl. Opt.*, vol. 52, pp. 4419-4425, 2013.

[35] X. Xia *et al.*, "A 360-degree floating 3D display based on light field regeneration," *Opt. Express*, vol. 21, pp. 11237-11247, 2013.

[36] T. Agocs *et al.*, "A Large Scale Interactive Holographic Display," *IEEE Virtual Reality Conference (VR 2006)*, pp. 311-311, 2006.

[37] J. Hahn, H. Kim, Y. Lim, G. Park, and B. Lee, "Wide viewing angle dynamic holographic stereogram with a curved array of spatial light modulators," *Opt. Express*, vol. 16, pp. 12372-12386, 2008.

[38] F. Aflatouni, B. Abiri, A. Rekhi, and A. Hajimiri, "Nanophotonic projection system," *Opt. Express*, vol. 23, pp. 21012-21022, 2015.

[39] L. J. Hornbeck, "Digital Light Processing and MEMS: an overview," *IEEE/LEOS 1996 Summer Topical Meetings*, pp. 7-8, 1996.

[40] C. R. Doerr, L. Chen, Y. Chen and L. L. Buhl. "Wide Bandwidth Silicon Nitride Grating Coupler," *IEEE Photonic Tech. L.*, vol. 22, pp. 1461-1463, 2010.

[41] A. Yaacobi, *Integrated Optical Phased Arrays for Lidar Applications*, PhD Dissertation, Massachusetts Institute of Technology, 2015.

[42] L. B. Soldano and E. C. M. Pennings, "Optical multi-mode interference devices based on self-imaging: principles and applications" *J. Lightwave Technol.*, vol. 13, pp. 615–627, 1995.

[43] S. Romero-García, F. Merget, F. Zhong, H. Finkelstein, and J. Witzens, "Silicon nitride CMOS-compatible platform for integrated photonics applications at visible wavelengths," *Opt. Express*, vol. 21, pp. 14036-14046, 2013.

[44] A. Gorin, A. Jaouad, E. Grondin, V. Aimez, and P. Charette, "Fabrication of silicon nitride waveguides for visible-light using PECVD: a study of the effect of plasma frequency on optical properties," *Opt. Express*, vol. 16, pp. 13509-13516, 2008.

[45] M. T. Wade, R. Kumar, K. Nammari, C. M. Gentry, J. Shainline, J. S. Orcutt, *et al.*, "Unidirectional chip-to-fiber grating couplers in unmodified 45nm CMOS Technology," in *Conference on Lasers and Electro-Optics*, 2014, p. STh3M.5.

[46] J. Notaros, F. Pavanello, M. T. Wade, C. Gentry, A. Atabaki, L. Alloatti, *et al.* "Ultra-Efficient CMOS Fiber-to-Chip Grating Couplers," in *Optical Fiber Communication Conference*, 2016, p. M2I.5.

[47] M. Fan, M. Popovic, and F. X. Kaertner, "High Directivity, Vertical Fiber-to-Chip Coupler with Anisotropically Radiating Grating Teeth," *Conference on Lasers and Electro-Optics (CLEO)*, paper CTuDD3, 2007.

[48] J. Sun, *Toward Accurate and Large-Scale Silicon Photonics*, PhD Dissertation, Massachusetts Institute of Technology, 2013.

[49] S. K. Cool, K. Breyne, E. Meyer, S. C. De Smedt and N. N. Sanders, "Comparison of In Vivo Optical Systems for Bioluminescence and Fluorescence Imaging," *J. Fluoresc.*, vol. 23, pp. 909-920, 2013.

[50] Z. Zhang, Z. You and D. Chu, "Fundamentals of phase-only liquid crystal on silicon (LCOS) devices," *Light Sci. Appl.*, vol. 3, 2014.

[51] H. Desmet, W. Bogaerts, A. Adamski, J. Beeckman, K. Neyts, and R. Baets, "Silicon-on-insulator optical waveguides with liquid crystal cladding for switching and tuning," *Proc. ECOC,* vol. 3, pp. 430-431, 2003.

[52] P. G. de Gennes and J. Prost, *The Physics of Liquid Crystals*, Oxford University Press, 1995.

[53] I. W. Stewart, *The Static and Dynamic Continuum Theory of Liquid Crystals*, Taylor and Fracnis, 2004.

[54] A. A. Sonin, *The Surface Physics of Liquid Crystals*, Gordon and Breach Publishers, 1995.

[55] R. A. Alla, *On the Control of Nematic Liquid Crystal Alignment*, PhD Dissertation, University of Gothenburg, 2013.

[56] J. He, "Polarity inversion driving method for liquid crystal display panel, driving apparatus and display device," U.S. patent 20150084941 A1, March 26, 2015.

[57] Y. Xing *et al.*, "Digitally Controlled Phase Shifter Using an SOI Slot Waveguide with Liquid Crystal Infiltration" *IEEE Photonic Tech. L.*, vol. 27, pp. 1269-1272, 2015.

[58] B. A. Block *et al.*, "Electro-optic polymer cladding ring resonator modulators," *Opt. Express*, vol. 16, pp. 18326-18333, 2008.

[59] J. Li, C. H. Wen, S. Gauza, R. Lu and S. T. Wu. "Refractive indices of liquid crystals for display applications," *J. Disp. Technol.*, vol. 1, pp. 51-61, 2005.